Department of Physics and Astronomy

University of Heidelberg

Master thesis

in Physics

submitted by

Dennis Weiser

2015

Measurement of jet fragmentation into charged particles in p-Pb collisions at $\sqrt{s_{\mathrm{NN}}} = 5.02$ TeV with ALICE

This Master thesis has been carried out by Dennis Weiser

at the

Physikalisches Institut Heidelberg

under the supervision of

apl. Prof. Dr. Klaus Reygers

Messung der Fragmentation von Jets in geladene Teilchen in p-Pb Kollisionen bei $\sqrt{s_{\mathrm{NN}}} = 5.02$ TeV mit ALICE:

Durch die Messung von Jets oder Jetstrukturobservablen in Blei-Blei Kollisionen können Rückschlüsse auf die Eigenschaften des Quark-Gluon Plasmas gezogen werden. Proton-Blei Kollisionen stellen ein wichtiges Referenzsystem dar, in welchem potentielle Anfangszustandseffekte oder Effekte kalter Kernmaterie berücksichtigt werden.
Wir präsentieren die Messung der longitudinalen Impulsverteilung von geladenen Teilchen mit Transversalimpuls $p_{\mathrm{T}} > 0.15$ GeV/c in geladenen Jets in Proton-Blei Kollisionen bei $\sqrt{s_{\mathrm{NN}}} = 5.02$ TeV unter Nutzung von Minimum Bias Daten und Daten, welche vom Übergangsstrahlungsdetektor (TRD) getriggered wurden. Durch Verwendung dieser Daten kann die Messung bis zu einem Transversalimpuls von $p_{\mathrm{T,\,jet}}^{\mathrm{ch}} = 120$ GeV/c erweitert werden. Geladene Jets werden mit dem anti-k_{T} Algorithmus mit Radiusparameter R=0.4 rekonstruiert. Der Abzug des Untergrundes wird sowohl auf Ereignisebene als auch auf Ereignisensembleebene durchgeführt.
Die gemessenen Fragmentationsverteilungen werden mit einer Referenz des PYTHIA Ereignisgenerators verglichen und zeigen keine starken Modifikation durch Kerneffekte.

Measurement of jet fragmentation into charged particles in p-Pb collisions at $\sqrt{s_{\mathrm{NN}}} = 5.02$ TeV with ALICE:

The measurement of jet energy loss or jet properties in lead-lead collisions allows to access the properties of the Quark-Gluon Plasma. Collisions of protons and lead ions provide an important reference system in which possible initial-state- or cold-nuclear-matter effects are present.
We present the measurement of the longitudinal momentum distribution of charged particles with transverse momentum $p_{\mathrm{T}} > 0.15$ GeV/c in charged jets in p-Pb collisions at $\sqrt{s_{\mathrm{NN}}} = 5.02$ TeV using minimum bias and Transition Radiation Detector (TRD) triggered data. Using the TRD triggered data the range of the measurement is extended up to $p_{\mathrm{T,\,jet}}^{\mathrm{ch}} = 120$ GeV/c. Charged jets are reconstructed with the anti-k_{T} algorithm with a radius parameter of R=0.4. The underlying event is subtracted event-by-event as well as on the event ensemble level.
The observed fragmentation distributions are compared to a reference from the event generator PYTHIA and indicate the absence of strong nuclear effects on jet fragmentation.

Contents

1 Introduction

1.1 Standard Model

During the last century tremendous progress has been made in the field of particle physics. Starting from the discovery of the atomic nucleus by Ernest Rutherford [1] physicists have been able to probe the very nature of atomic nuclei on smaller and smaller scales. As protons and neutrons were identified as the constituents of atomic nuclei it seemed natural to ask what would hold them together, since the only force acting between those should be electromagnetic repulsion (gravitational attraction is negligible at the level of atomic nuclei). The first one to come up with a significant theory that would explain a binding between nucleons (protons and neutrons) was Hideki Yukawa [2]. He suggested that protons and neutrons are held together by some sort of field analogous to an electromagnetic field, in which the quanta of the field are electrically charged and have about 200 times the mass of an electron. With the discovery of pions in cosmic rays it was believed that these should be the particles described by Yukawa that mediate the strong interaction between nucleons.
When more and more seemingly elementary particles were observed Murray Gell-Mann introduced the so-called Eightfold Way [3]. This basically is a scheme with which one could put the existing particles into order in geometrical objects like hexagons or triangles depending on properties like isospin or strangeness. These symmetry considerations were powerful since they led, for instance, to the prediction of the Ω^- baryon.
In addition they led to the postulation of the quark model, which offered an explanation to the question why all the particles fit into these geometrical shapes. The quark model states that baryons consist of three quarks and mesons consist of two quarks, one quark and one anti-quark. All known particle species to that date could be constructed by combining the three known quark types ('flavors'): Up, down and strange.

However, this prevailing paradigm was shattered in the 'November Revolution' 1974 when the groups of Burton Richter [4] and Samuel Ting [5] announced the observation of a new particle whose properties could not be explained with the existing three flavor quark model. The existence of a fourth quark had been predicted before [6], but the discovery of this particle, which became later known as J/ψ, delivered the proof. Over the years two even heavier quarks have been discovered: They are known today as the beauty (or bottom) [7] and top quark [8].

On the way to all the known elementary particles today there were also other important discoveries like the W and Z bosons, the mediators of the weak force.

The last great milestone in modern particle physics was the discovery of a boson consistent with the standard model higgs boson in 2012 by the ATLAS and CMS collaborations [9], [10].

All elementary particles that are known today are summarised in Fig. 1.1.

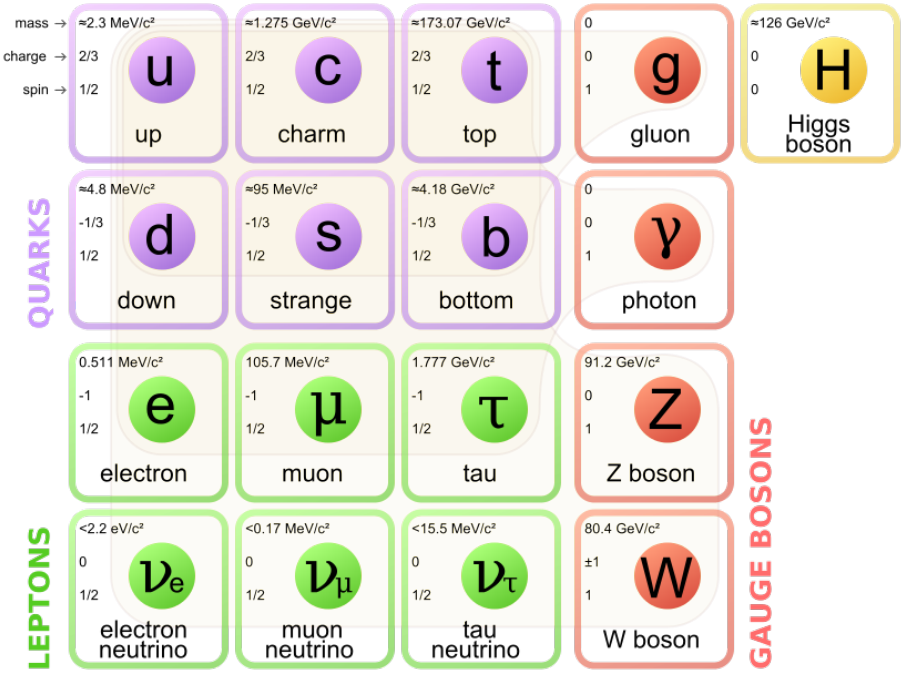

Figure 1.1: Overview of the elementary particles described in the Standard Model [11].

All these elementary particles known today and their interactions are described by the Standard Model of Particle Physics. Quarks and leptons are fundamental fermions which are the building blocks of matter. Gauge bosons mediate the interactions. The Higgs boson is connected to the mass-generation of elementary particles via electroweak symmetrybreaking.

The Standard Model is a gauge-invariant quantum field theory with gauge group $SU(3) \times SU(2) \times U(1)$. It comprises the theory of electroweak interaction and the theory of strong interaction: Quantum Chromodynamics.

The theory of electroweak interaction arose from the unification of the theories of electromagnetism and weak interaction [12], [13], [14], [15].

Since hadronic collisions can be described by Quantum Chromodynamics it will be the focus of the next section.

1.2 Quantum Chromodynamics

Quantum Chromodynamics (QCD) is the theory of strong interaction and it describes the interactions between quarks and gluons. Quarks are the fundamental constituents of nuclei and gluons are the mediators of the strong force. QCD is formulated as a non-abelian gauge theory with gauge group SU(3). This implies that gluons can interact with each other, which is a fundamental difference to the electromagnetic force. There, the carriers of the force (photons) only interact with the fundamental fermions and not with themselves since they do not carry electric charge. The analogy to electric charge is colour charge in QCD. The measurement of the cross-section of $e^+e^- \rightarrow$ hadrons suggested that quarks have an additional degree of freedom which was introduced later as colour-charge. Quarks carry colour charge whereas gluons carry colour and anticolour charge.

The strong coupling α_s, defined by a physical process (e.g. scattering), depends on the momentum transfer Q of the process. Figure 1.2 shows that the coupling tends to zero as the momentum transfer grows. This phenomenon is known as asymptotic freedom and is a key feature of QCD. Since high momentum transfer can be translated into high spatial resolution the strong coupling vanishes at short distances. At lower momentum transfer the strong coupling gets larger, where the scale at which it is of order 1 is the hadronic scale $\Lambda_{\mathrm{QCD}} \approx 200$ MeV.

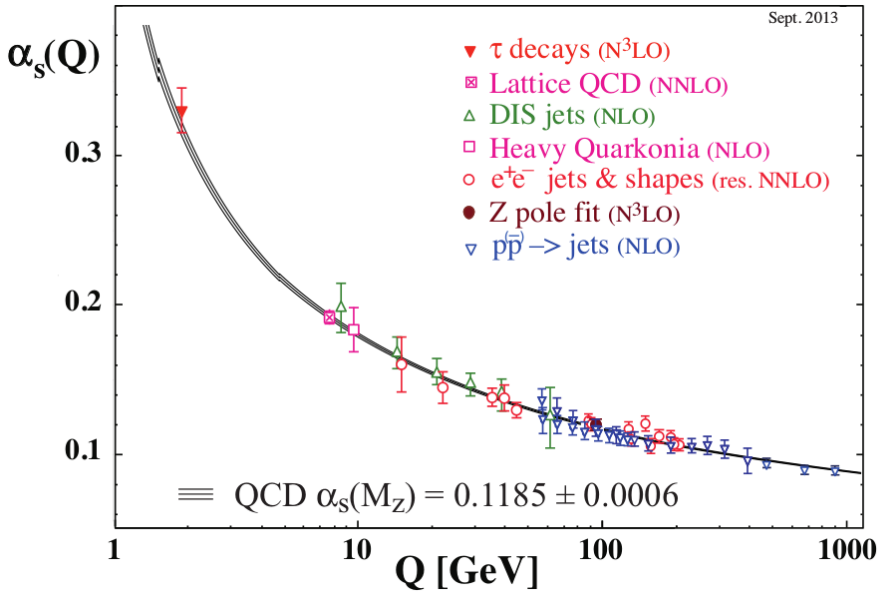

Figure 1.2: Measurements of α_s with corresponding order of perturbation theory used for extraction [16].

This Q dependence of the coupling divides QCD into two regimes: Perturbative QCD ($Q \gg \Lambda_{\mathrm{QCD}}$) and nonperturbative QCD ($Q \approx \Lambda_{\mathrm{QCD}}$). In the regime of

perturbative QCD Matrix Elements for given processes are calculable by Taylor expansion of full QCD in orders of α_s using a cutoff at a certain order. For lower Q, e.g. higher α_s, this procedure breaks down eventually due to the non-convergence of the expansion series. In this regime one is restricted to phenomenological models or universal functions measured in experiments (parton densities, form factors, etc.). A different approach towards solving QCD in this regime is Lattice QCD. There full continuum QCD is approximated by full QCD on a space-time grid with a finite grid point distance and finite volume, such that the continuum and infinite volume limit is full QCD.
One important result of 'quenched' (no gluon splittings) Lattice QCD is that the potential between a colour charge and an anti-colour charge grows linearly when the two charges are separated more than about a femtometer [17]. The phenomenological QCD potential between a quark and an antiquark is given by

$$V(r) = -\frac{4\alpha_s}{3r} + kr, \tag{1.1}$$

with the distance r between both quarks and $k \approx 1$ GeV fm^{-1} being a phenomenological constant.
This explains the so-called confinement phenomenon, i.e. quarks can never be observed freely, but only 'trapped' in hadrons: As one tries to separate both quarks the potential energy of the colour field grows since the distance r grows. At some point it will be energetically favourable to produce a new quark-antiquark pair out of the vacuum, so that one is left with two hadrons (see Fig. 1.3).
Staying in this simplistic picture one can easily understand the production of jets in e^+e^- - collisions. Consider the high-energy process $e^+e^- \to \gamma^*/Z \to q\bar{q}$. Due to momentum conservation the outgoing quarks will have to propagate in opposite directions. Their high energy will result in a cascade of string breaks, thus leading to two collimated sprays of hadrons in opposite directions: jets. The additional radiation of a hard gluon by one of the quarks will lead to a third jet, as first reported by collaborations at the PETRA collider 1979/80 [18], [19], [20], [21]. Hadronisation models implemented in modern event generators (for instance PYTHIA [22] uses the Lund Model [23]) are based on these string breaking mechanisms, but are of course more sophisticated and make quantitative predictions.

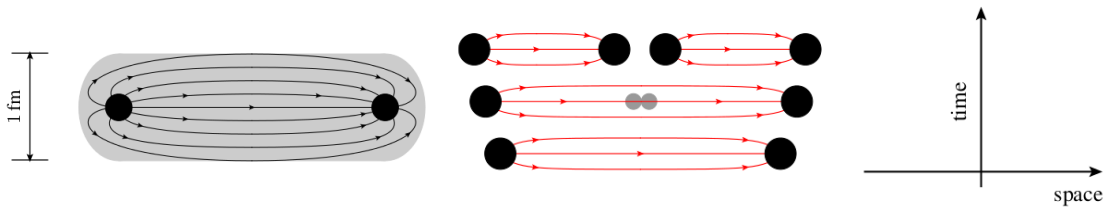

Figure 1.3: String-like colour field between two QCD charges (left) and schematic space-time evolution of string breaking (right) [24].

Jets can also be produced in highly energetic hadron collisions. There they arise from the hard scattering of two partons (parton: quark or gluon) and their subsequent fragmentation into hadrons. The term fragmentation usually refers to (perturbative) parton splitting processes and the (nonperturbative) hadronisation. The production cross-section of jets or hadrons in hadron collisions is calculable by applying the QCD factorisation theorem [25]. It allows the subdivision of the different involved processes into a short-range perturbative part and a long-range nonperturbative part, which is illustrated in Fig. 1.4. The acronyms ISR and FSR refer to possible initial or final state radiation.

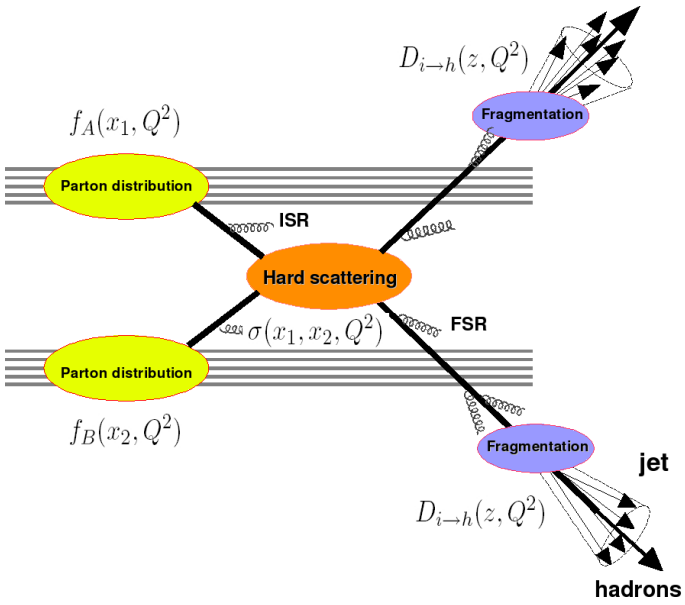

Figure 1.4: Visualisation of dijet production and QCD factorisation [26].

The production cross-section of a (high p_{T}) hadron h produced in a collision of hadron A and B can then be written as:

$$d\sigma^{\mathrm{hard}}_{\mathrm{AB}\to\mathrm{h}} = f_{\mathrm{a/A}}(x_1,Q^2)\otimes f_{\mathrm{b/B}}(x_1,Q^2)\otimes d\sigma^{\mathrm{hard}}_{\mathrm{ab}\to\mathrm{c}}(x_1,x_2,Q^2)\otimes D_{\mathrm{c}\to\mathrm{h}}(z,Q^2), \quad (1.2)$$

in which

- $f_{\mathrm{a/A}}(x_1,Q^2)$ is the parton distribution function (PDF) which encodes the probability to find parton a with a certain momentum fraction x in hadron A,
- $d\sigma^{\mathrm{hard}}_{\mathrm{ab}\to\mathrm{c}}(x_1,x_2,Q^2)$ is the perturbatively calculable cross-section of the hard scattering of parton a and b,
- $D_{\mathrm{c}\to\mathrm{h}}(z,Q^2)$ is the fragmentation function (FF) that yields the probability that the outgoing parton c fragments into a hadron h with momentum fraction $z = p_{\mathrm{hadron}}/p_{\mathrm{parton}}$.

Parton distribution functions and fragmentation functions are nonperturbative objects and need to be measured in experiments like deep inelastic $e^{\pm}$ - nucleus collisions (PDFs) or e^+e^- - collisions (FFs).

In order to understand the dynamics of heavy-ion collisions and the behaviour of jets therein we need to focus on the continuum part of QCD and on the Quark-Gluon Plasma in particular. In the next section the different phases of strongly interacting matter will be introduced and afterwards we will motivate possible jet observables that are expected to give insights to the properties of the Quark-Gluon Plasma.

1.3 Heavy-Ion Collisions and the Quark-Gluon Plasma

Ultrarelativistic heavy-ion collisions offer the possibility to study QCD in extreme conditions of temperature, density and small parton momentum fraction x. The collision of highly energetic heavy nuclei is expected to form a hot and dense medium in that quarks and gluons are deconfined. Indeed Lattice QCD calculations predict a new state of matter consisting of deconfined quarks and gluons above a critical temperature of $T_{\text{crit}} \approx 170$ MeV [27] (for two quark flavors), the Quark-Gluon Plasma. This state of matter is believed to have permeated the early universe until around 10 µs after the big bang, when a phase transition to ordinary nuclear matter occurred. Depending on the order of the phase transition different cosmological implications have been postulated [28]. Therefore it is of particular importance for our understanding of QCD and the evolution of the universe to study and characterise this state of matter and its phase transitions.

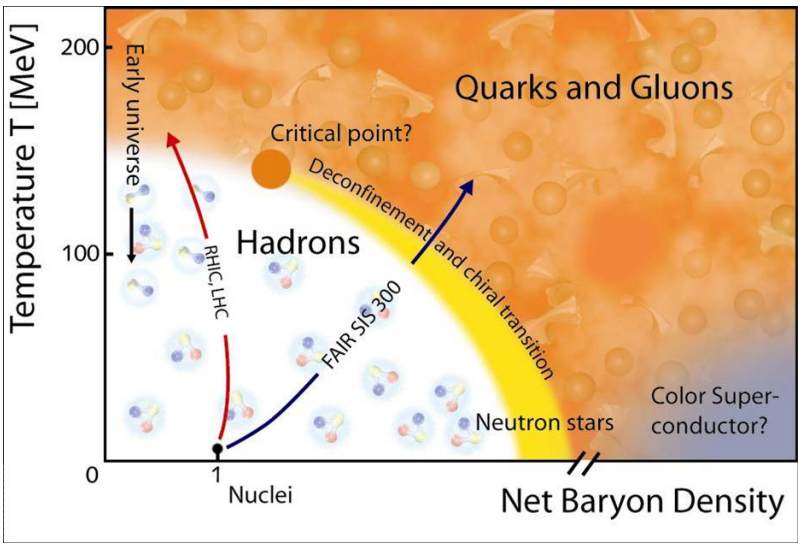

Figure 1.5: Sketch of the QCD phase diagram [29].

Figure 1.5 shows a sketch of the phase diagram of strongly interacting matter to

the best of our knowledge. It shows the different states of hadronic matter depending on temperature and net baryon density, where a net baryon density of 1 at low temperature corresponds to ordinary nuclear matter as present in atomic nuclei. The phase transition which occurred in the early universe is indicated at small net baryon density. The experiments at the Relativistic Heavy-Ion Collider (RHIC) and the Large Hadron Collider (LHC) aim for studying the phase transition at low net baryon density. Experiments at the future SIS 300 storage ring at the Facility for Antiproton and Ion Research (FAIR) at the GSI Helmholtz Center for Heavy-Ion Research aim for studying the phase transition at higher net baryon density. Matter of high net baryon density and low temperature is believed to exist in neutron stars. In this regime it is expected that quarks build diquark pairs to form a colour superconductor at low temperature, analogous to superconductivity in solid state physics. Unfortunately this regime is currently out of experimental reach.

To study and characterise the hot and dense medium created in high-energy nucleus-nucleus (AA) collisions typically production cross-sections of different observables are compared to those obtained in scaled proton-nucleus (pA) or proton-proton (pp) collisions. The nuclear modification factor R_{AA} reads:

$$R_{\mathrm{AA}}(p_{\mathrm{T}}, y; b) = \frac{d^2N_{\mathrm{AA}}/dydp_{\mathrm{T}}}{\langle T_{\mathrm{AA}}(b)\rangle d^2\sigma_{\mathrm{pp}}/dydp_{\mathrm{T}}}, \tag{1.3}$$

with the transverse momentum p_{T}, rapidity y and the impact parameter b. The variable $T_{\mathrm{AA}}(b)$ is the nuclear overlap function which arises from the binary collision scaling of the reference system. Nucleus-nucleus collisions are there treated as independent collisions of nucleons which is modelled by the Glauber Model. For a recent review see [30]. The nuclear modification factor for proton nucleus collisions R_{pA} is defined analogously.

Deviations in the nuclear modification factors from 1 can be related to the properties of the medium ('hot QCD medium' in AA collisions and 'cold QCD medium' in pA collisions).
There are a lot of different observables that are expected to shed light on the properties of the Quark-Gluon Plasma. An overview can be found in textbooks like [31], [32]. Observables connected to jets will be explained in the next section.

1.3.1 Jets in Heavy-Ion Collisions

In heavy-ion collisions hard parton scatterings occur on smaller time scales than the formation of medium. Thus hard partons created in those processes will have to penetrate the evolving medium and will potentially be affected by it. It was first proposed by Bjorken that highly energetic partons should experience energy loss in the created medium [33]. His initial idea was that when a hard parton pair is produced at the edge of the overlap zone of the two colliding nuclei one of them could escape the medium nearly unaffected while the other will traverse through almost the entire volume (see Fig. 1.6).

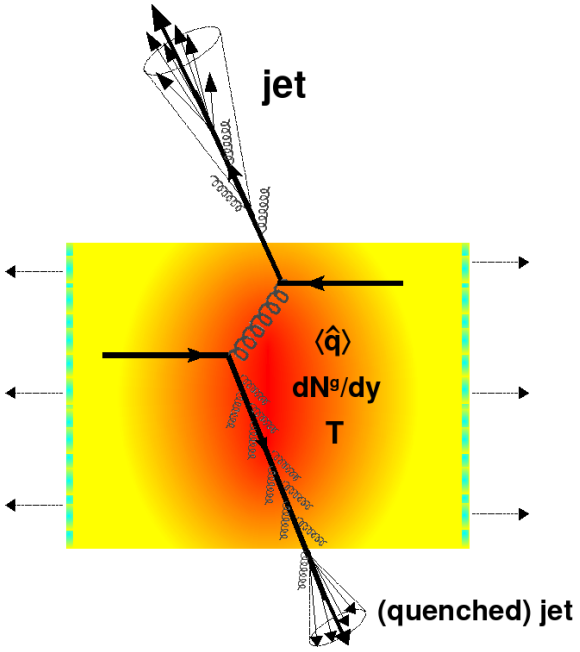

Figure 1.6: Energy loss of a hard parton in the medium [26].

Since hard partons are observable as jets he concluded that one of the jets will be observed with significantly less transverse momentum than the other, or not be observable at all, which would be a clear indication of the formation of a hot and dense medium. This phenomenon is known as 'jet quenching' and was first observed at RHIC [34], [35]. While Bjorken assumed that elastic collisions of the parton with the medium constituents are the source of the energy loss, modern calculations show that at sufficiently high parton momentum the radiation of gluons is the dominant effect [36].
This parton energy loss is experimentally observable via the suppression of high p_{T} hadrons or jets. Also, due to different in-medium pathlength of the initial partons dihadron or dijet back-to-back pairs will be observed with unbalanced momentum. Furthermore, the medium-induced gluon radiation is expected to lead to a modification of the the particle momentum distribution inside jets. The suppression

of high p_T hadrons or jets is typically investigated with the R_{AA} variable which was already defined in 1.3.

While the R_{AA} basically compares the number of jets in pp-collisions and AA-collisions, jet structure observables are more differential. It has been predicted that the medium induced gluon radiation should lead to a modification of the parton fragmentation [37], [38]. Thus jet shapes, multiplicities and intrinsic momentum distributions should be modified in AA-collisions. A typical variable for studying momentum distributions in jets is $z = p_{\mathrm{hadron}}/p_{\mathrm{jet}}$ or $\xi = \ln(1/z)$, respectively. The ξ variable shows the so-called hump-backed plateau (see Fig. 1.7) for which modifications in AA-collisions have been predicted [39] and also recently observed [40], [41].

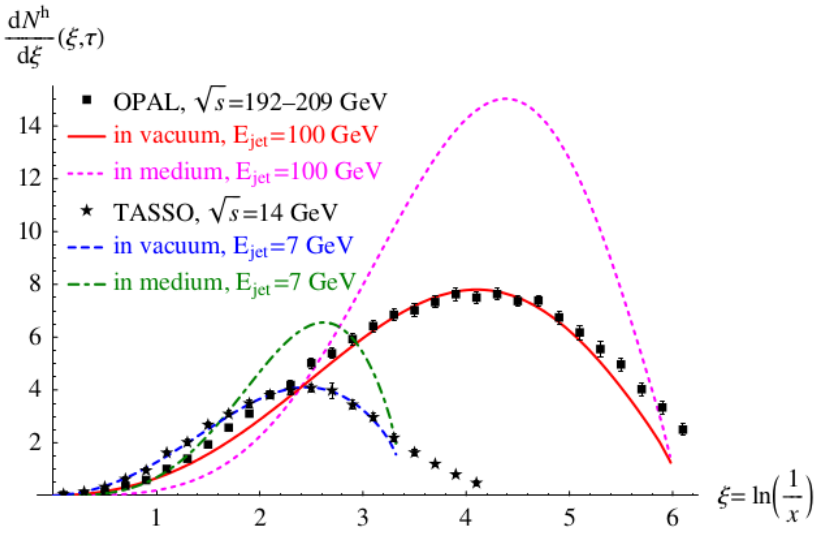

Figure 1.7: dN/dξ distribution for data from e^+e^- collisions and model calculations. For the latter a comparison of vacuum and in-medium fragmentation is shown [39].

1.4 Proton-Nucleus Collisions

The study of proton-nucleus collisions provides an important baseline to nucleus-nucleus collisions. Since in p-A-collisions a formation of the Quark-Gluon Plasma is not expected the measurement is crucial to disentangle the effects arising from the hot and dense medium and those related to the nucleus itself.
Effects that are expected to play a role in proton-nucleus collisions are the modification of the parton distribution in the nucleus [42], [43] and also the impact of multiple scatterings and hadronic re-interactions in the initial and final state is discussed [44], [45].

So far measurements of jets in p-Pb with ALICE show no modification in R_{pPb} as well as in the observed jet structure compared to pp collisions [46], [47]. Figure 1.4 (left panel) shows the nuclear modification factor for charged jets measured with ALICE and the ratio of jets reconstructed with different radius parameters (right panel). The latter is sensitive to the fragmentation of the jets. Both observables show no modification in p-Pb compared to pp.

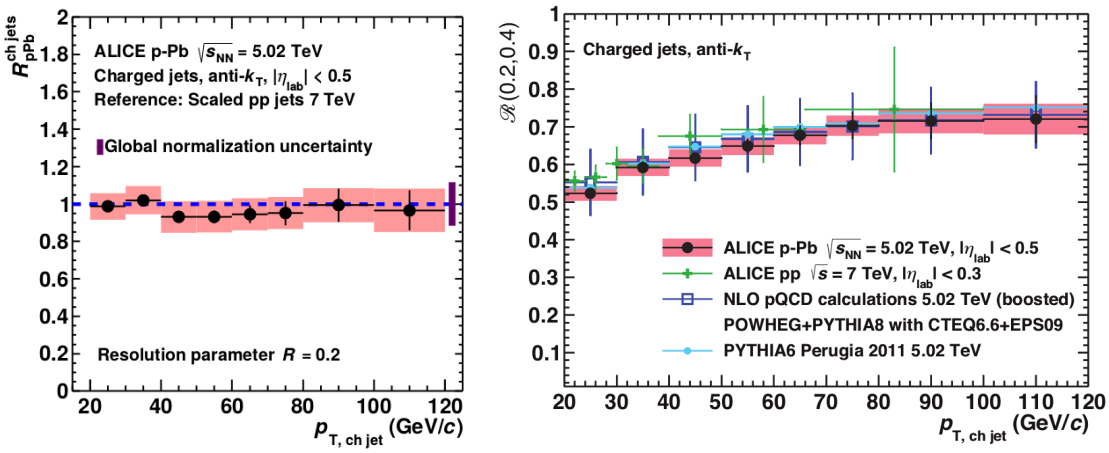

Figure 1.8: Nuclear modification factor (left) and ratio of jets reconstructed with radius parameters of 0.2 and 0.4 (right) [46].

However, the reported ratio of jet spectra reconstructed with different radius parameters is not very differential. So it is the goal of the analysis reported in this thesis to measure the (more differential) fragmentation distribution in p-Pb-collisions up to the highest jet momenta accessible with ALICE. The p_T range covered by minimum bias data will be extended using the jet trigger provided by the Transition Radiation Detector.
A description of ALICE and the subdetectors used in this analysis follows in the next section.

2 A Large Ion Collider Experiment at the LHC

2.1 The CERN Large Hadron Collider

The Large Hadron Collider (LHC) is a superconducting hadron accelerator and collider located at the 26.7 km tunnel inherited from the Large Electron Positron Collider (LEP). It is located close to Geneva in Switzerland and lies between 45 m and 170 m below ground [48]. Unlike for particle-antiparticle colliders the counter-rotating proton beams can not share the same ring. Therefore the LHC consists of two rings, one for each proton direction, both situated inside the same cryostat. Two sets of superconducting magnets provide an opposite magnetic field for both beams with a peak dipole field of 8.33 T corresponding to a design proton-proton center of mass energy of 14 TeV.
The injection chain, that delivers the protons as so-called bunch trains into the LHC, is described elsewhere [48]. Already existing structures like the Proton Synchrotron (PS) and the Super Proton Synchrotron (SPS) are used to pre-accelerate the ion bunches before injection into the LHC beam lines. For proton proton operation it is foreseen to have 2808 bunches of protons with a bunch spacing of 25 ns in each beam. In the LHC the ions are accelerated to their final energy and are brought to collision at four distinct points, the nominal interaction points (see Fig. 2.1).

There are four major experiments with different physics objectives built up around those interaction points:

- ATLAS and CMS are high luminosity pp experiments which are mainly interested in the study of electroweak symmetry-breaking and search for new physics.
- LHCb is a dedicated B-physics experiment interested in measurements of CP violation using lower luminosity.
- ALICE runs also at lower luminosity and the physics interest and experimental setup will be explained in the following.

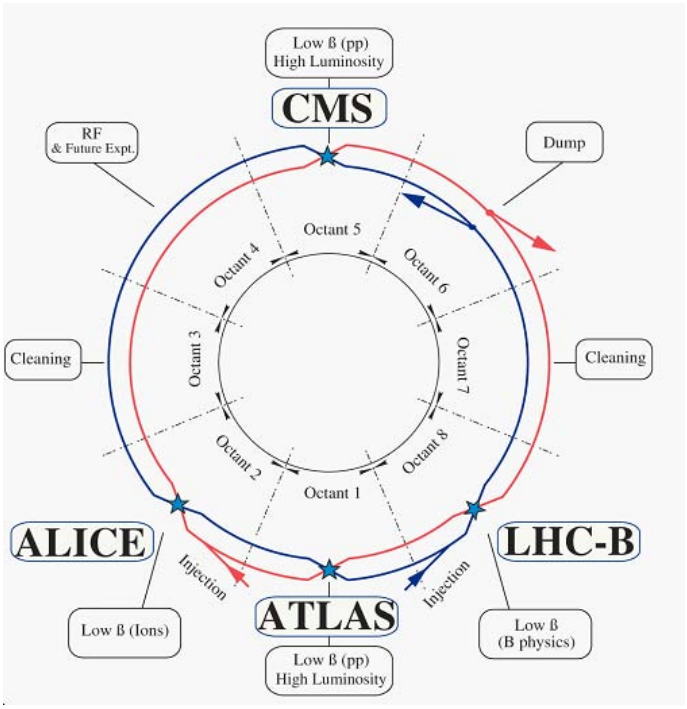

Figure 2.1: Schematic view of the LHC beam lines and main experiments [48].

2.2 Overview of the ALICE Detector

A Large Ion Collider Experiment (ALICE) is a dedicated heavy-ion experiment and is focused on QCD measurements, especially the study of the hot and dense medium that is created in ultrarelativistic heavy-ion collisions. ALICE is built by a collaboration of 1550 members from 151 institutes from 37 countries [49]. The overall size of the detector is $16 \times 16 \times 26$ m^3 and its weight is about 10 000 t. ALICE consists of a central barrel part which is located in the magnet inherited from the L3 experiment and a forward muon arm. The central barrel contains, from the inside out, an Inner Tracking System (ITS), a cylindrical Time-Projection Chamber (TPC), a Transition Radiation detector (TRD), a Time-of-Flight detector (TOF), a Ring Imaging Cherenkov detector (HMPID) and two electromagnetic calorimeters (EMCal and PHOS). At small angles, different smaller detectors have been placed for event characterisation and triggering (ZDC, PMD, FMD, T0, V0). An overview of the ALICE detector is shown in Fig. 2.2.

In the following the subsystems that are used in this analysis will be discussed in more detail. In addition the electromagnetic calorimeters connected to jet measurements will be briefly discussed. A comprehensive overview of all subdetectors can be found in [51].

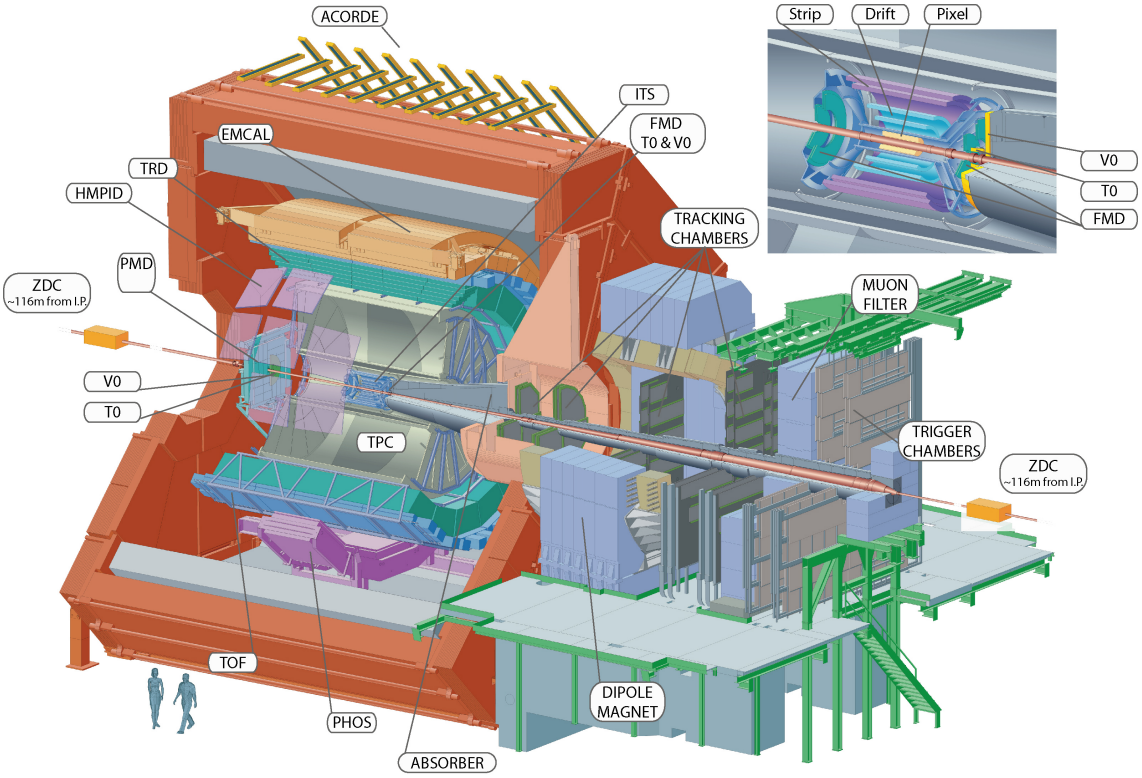

Figure 2.2: Schematic view of the ALICE detector [50].

2.2.1 Inner Tracking System

The Inner Tracking System (ITS) consists of six layers of silicon detectors that are located at radii between 4 cm and 43 cm around the beam pipe, as shown schematically in Fig. 2.3. It covers a pseudorapidity range of $|\eta| < 0.9$ and has full azimuthal coverage. The innermost layer has a more extended pseudorapidity coverage ($|\eta| < 1.98$) for multiplicity measurements. Since the charged particle multiplicity density decreases with increasing distance from the beampipe the layers have increasing granularity towards the beam pipe. The two innermost layer are Silicon Pixel Detectors (SPD), the following two layers are Silicon Drift Detectors (SDD) and the outermost two are Silicon Strip Detectors.
The main tasks of the ITS are the localisation of the primary vertex, the reconstruction of secondary vertices from D, B meson and hyperon decays and to improve the momentum and angle resolution for tracks reconstructed in the TPC. Furthermore it can be used for identification of particles with momentum below 200 MeV/c and for tracking of particles that traverse dead regions in the TPC.
In this analysis the ITS is used to improve the momentum resolution of TPC tracks and to reduce the contribution from tracks arising from secondaries as well as pile-up events.

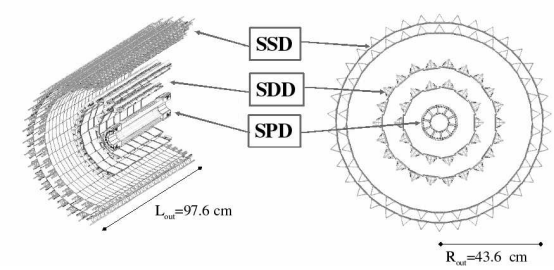

Figure 2.3: Geometry of the Inner Tracking System [51].

2.2.2 Time-Projection Chamber

The Time-Projection Chamber (TPC) is the main tracking device in the ALICE central barrel and it provides also excellent charged particle identification. It covers the full azimuth (except for dead regions due to support structures) and the pseudorapidity of $|\eta| < 0.9$ for tracks with full radial track length. It has a cylindrical shape with an inner radius of about 85 cm, an outer radius of about 250 cm and a length in beam direction of 5 m. The structure of the TPC is shown in Fig. 2.4.

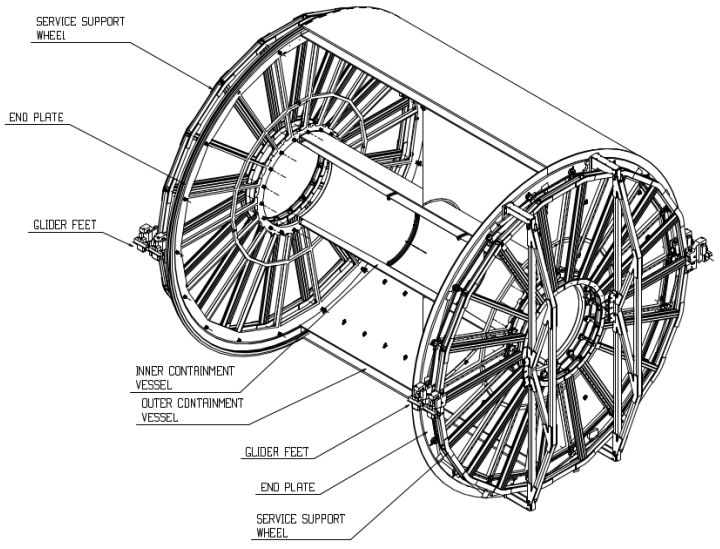

Figure 2.4: Geometry of the TPC [51].

The chamber was filled with a Ne/CO_2 mixture during the data taking periods relevant for this analysis. The electric drift field is created between the central high voltage electrode and the anode wires which are located at the endcaps. Incoming charged particles will produce primary ionisation electrons along their path. These electrons then drift towards the endcaps where they are amplified and detected. The endcaps consist of Multi-Wire-Proportional-Chambers with adjacent cathode pads.

The pad readout yields two dimensional position information of the tracks. The third position dimension comes from the measurement of the drift time.
In addition the ionisation signal is proportional to the energy lost by the primary particle (dE/dx) and thus it can provide information about the particle species. However, in this analysis the excellent particle identification capabilities of the TPC will not be exploited, since it will be only used for tracking.
A limiting factor of the TPC in terms of luminosity is the long drift time (≈ 90 µs) which corresponds at an interaction rate of about 350 kHz and at a typical pp luminosity of 5×10^{30} cm^{-2} s^{-1} to about 60 pp interactions. Therefore care has to be taken to reject tracks arising from 'past' or 'future' events using ITS based methods.

2.2.3 Transition Radiation Detector

The main task of the Transition Radiation Detector (TRD) is to provide electron-pion separation for momenta above 1 GeV/c. This is based on the radiation of transition radiation photons by highly relativistic ($\gamma > 1000$) charged particles which is released when they pass through a radiator material that comprises many layers of this material. For the ALICE TRD a carbon fibre laminated Rohacell/polypropylene fibre sandwich radiator foam is used to introduce many layer transitions naturally.
The TRD consists of 18 supermodules each containing five TRD stacks in which one stack contains six TRD chambers. One chamber consists of a radiator, a gas (Xe/CO_2 (85:15)) filled drift volume and multi-wire proportional chambers with pad readout. The pseudorapidity coverage is $-0.9 < \eta < 0.9$ and the nominal azimuthal coverage is 2π. Figure 2.5 shows the final design of the TRD and the installation status during the years 2012/13 which are relevant for the data analysed in this work. As can be seen from the figure five TRD supermodules were not yet installed at that time which reduced the azimuthal coverage. The TRD was finally completed in 2014.

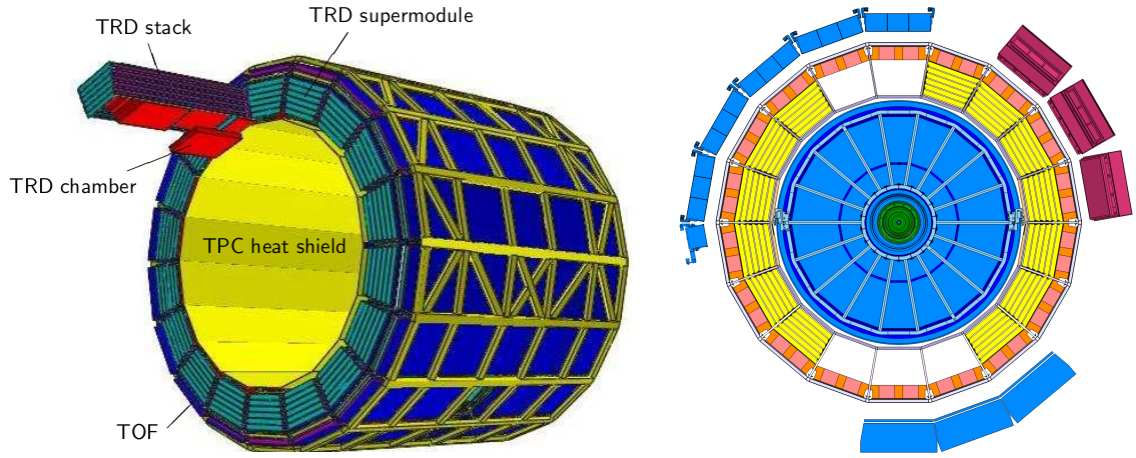

Figure 2.5: Geometry of the TRD (left) and TRD (shown in yellow) installation status 2012/13 (right) [51; 50].

When a charged particle enters a TRD chamber it produces electrons in the counting gas via ionisation. In addition, particles exceeding the threshold for transition radiation production ($\gamma > 1000$) will produce X-ray photons when they pass the radiator. These photons will also be converted in the gas, but most likely at the beginning of the drift region. All produced electrons will drift towards the anode wires and produce a gas amplification which can be read-out at the readout pads. Figure 2.6 shows schematically the production of primary ionisation in the drift region for pions and electrons, for electrons additional transition radiation photons will ionise the gas at the beginning of the drift volume.

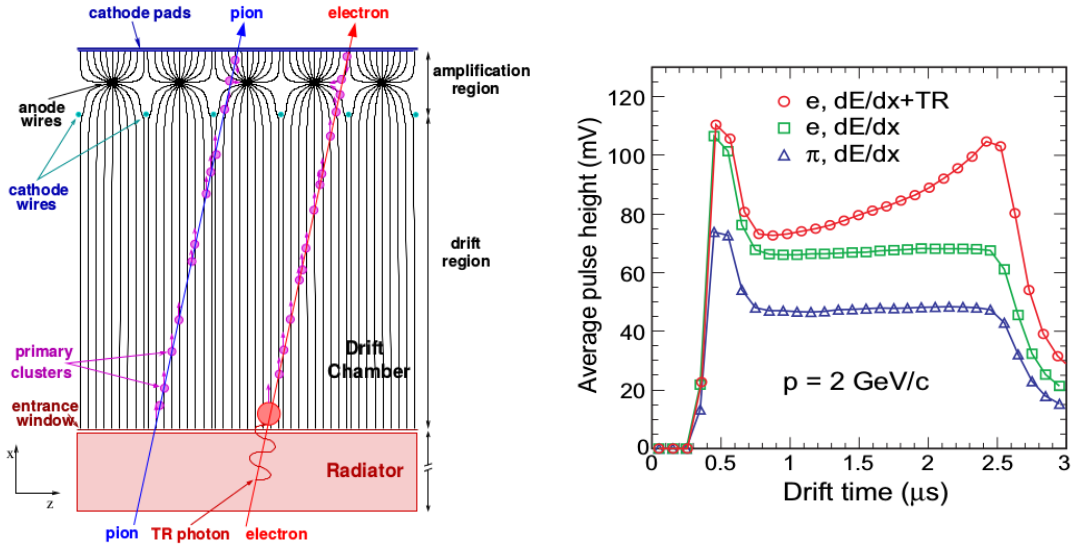

Figure 2.6: Schematic view of a TRD chamber in the $r\phi$ plane (left) and average pulse height versus drift time for electrons (with and without radiator) and pions for momenta of 2 GeV/c (right) [51].

As can also be seen the average energy loss of 2 GeV/c electrons (with and without transition radiation) is higher than for pions with the same momentum. Since the transition radiation will ionise the gas at the very beginning of the drift region, these electrons will arrive last at the anode wires. This leads to the characteristic peak for electrons with transition radiation at large drift times in Fig. 2.6. The peak at small drift times is caused by the stronger gas amplification near the anode wires in the amplification region. Making use of these energy loss signals an efficient discrimination between pions and electrons can be accomplished.
In addition to the particle identification capabilities the TRD can also be used for triggering. In this thesis the TRD jet trigger is used and will be explained in Sec. 2.3.

2.2.4 Electromagnetic Calorimeters

ALICE comprises three electromagnetic calorimeters, two of which are specifically designed for jet measurements: EMCAL [52] and DCal [53].

The EMCAL covers $|\eta| < 0.7$ in pseudorapidity and 110 degrees in azimuth. Technically it is a layered Lead-Scintillator sampling calorimeter. It is designed to provide fast triggers on high energy jets, measurements of neutral jet energy and an improvement of jet energy resolution.

To extend the physics capabilities of EMCAL the Di-jet Calorimeter (DCal) was installed in 2014. It covers 60 degrees in azimuth and also $|\eta| < 0.7$. It enables measurements of back-to-back correlations which are impossible with the EMCAL alone (see Fig. 2.7).

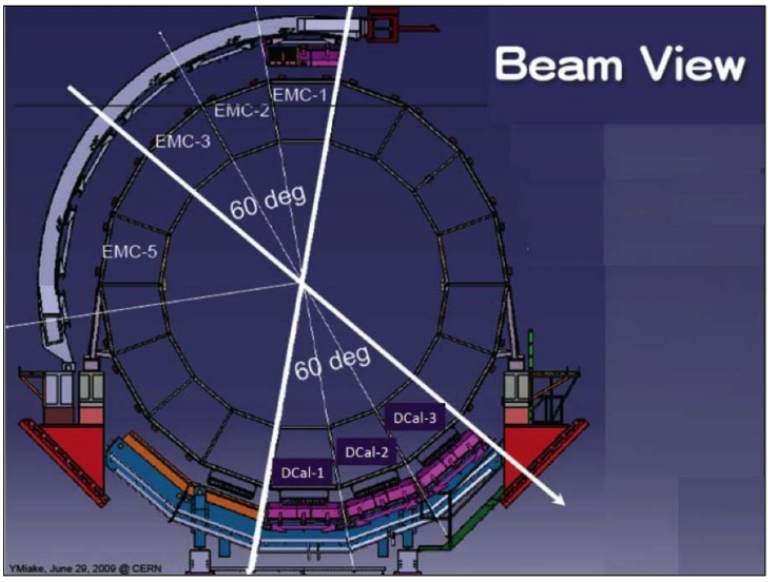

Figure 2.7: View in beam direction. The back-to-back placement of EMCAL (upper part) and DCal (lower part) can be seen [53].

DCal is built from six DCal super modules, but also contains three super modules of the existing PHOS [54] calorimeter.

Calorimeters are in principle capable of reconstructing the full jet energy, but the momenta of the charged particles in the jet are inaccessible with electromagnetic calorimetry alone. In order to measure the momentum distributions of the tracks in the jet a different approach can be used and will be explained in Sec. 2.5.

2.3 Trigger System

Triggering is crucial for jet analyses at hadron colliders since hard collisions, which are of most physics interest, occur much more rarely than soft collisions. ALICE comprises several detectors capable of delivering fast signals, which can be used as input to the trigger logic. The trigger decision is generated by the Central Trigger Processor (CTP) [55] based on the input signals from different detectors and information about the bunch crossings.
In ALICE three levels of hardware triggers are used: Level 0, 1, 2. The Level 0 (L0) decision is made ~ 0.9 µs after the interaction using inputs from fast detectors like scintillators or silicon pixel detectors. The events that got accepted at L0 are evaluated further based on the inputs from TRD, EMCal and ZDC to arrive at a Level 1 (L1) decision ~ 6.5 µs after the interaction. After about 100 µs (corresponds to the drift time of the TPC) a Level 2 (L2) decision is made and the data of the accepted events are sent to the High Level Trigger (HLT) and Data-Acquisition System (DAQ) where event building and data reduction takes place. In LHC Run 1 all L1 events were also accepted at L2. In the future the L2 decision might be used for instance for pile-up rejection.
The ALICE trigger system is described in detail in [51; 55]. An up-to-date version of the different detector inputs to the trigger logic (trigger classes) can be found in [56]. In the following we want to focus on the trigger classes used in this analysis.

Minimum Bias Trigger
A minimum bias trigger is the least rejective trigger and delivers the least biased data sample. The minimum bias trigger used in this analysis is derived from a coincident signal in the forward ($2.8 < \eta < 5.1$) and backward ($-3.7 < \eta < -1.7$) scintillator arrays V0A and V0C.

TRD Jet Trigger
The TRD provides triggers on electrons from quarkonia and open beauty decays and also on charged jets. These triggers are based on tracks reconstructed on-line in the TRD. In each of the six TRD layers in one stack track segments (tracklets) can be reconstructed and shipped to the Global Tracking Unit (GTU) which matches those tracklets based on their position. A track is formed from at least four tracklets that are consistent with a track pointing to the primary vertex. The transverse momentum p_{T} of the track is extracted from a straight line fit through the tracklet position in transverse direction [57]. The transverse offset of the straight line fit from the nominal interaction point then translates into the transverse momentum of the track. The PID information for a given track is obtained from the layer-averaged deposited charge of the tracklets that form this track.
For the jet trigger the p_{T} and the position of the tracks is used. A TRD stack is comparable in size to a typical jet cone ($R \approx 0.2$). Since the number of tracks in a jet grow with the transverse momentum of the jet this motivated the trigger condition of at least three tracks above 3 GeV/c in any TRD stack.

2.4 Data Reconstruction

After the data processing in the DAQ the raw data have to undergo several reconstruction steps in order to be usable for analyses. To accomplish this the ROOT [58] based framework AliRoot [59] has been developed. It provides the necessary tools for event reconstruction, but it also provides access to Monte-Carlo (MC) event generators like Pythia and Hijing and also the simulation of the detector geometry and response via Geant or Fluka. In Fig. 2.8 the processes for the data reconstruction are shown schematically. The experimental raw data are translatable into digitised detector signals (digits). The reconstruction can then be performed directly on the raw data or on the digits. The output from Monte Carlo simulations is available as digits and can be treated likewise.

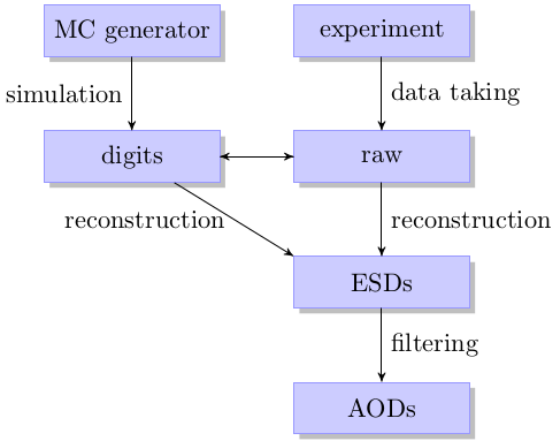

Figure 2.8: Steps in raw data processing [60].

The main part of the reconstruction is the tracking in the central barrel. Figure 2.9 shows the different steps involved in the track reconstruction. The tracking starts with a cluster finding procedure that is performed in each detector. A cluster is a set of adjacent (in space or time) digits which is presumably produced by the same particle. Next, a preliminary interaction vertex is reconstructed from clusters in the SPD, assuming that the primary vertex is the point to which most clusters point. After that the global tracking is performed using an inward-outward-inward scheme. It starts with the track finding in the TPC, starting at large radii. Track candidates are subsequently propagated inward to finally arrive at the outermost ITS layer. These are then used as seeds for the track finding in the ITS where they are also propagated inwards. When the ITS tracking is done the tracks are propagated outward and refitted with a Kalman filter [61]. If possible the tracks

are matched with tracklets or signals in the outer detectors. As a final step and for optimal momentum resolution the tracks are propagated inwards from the outer radius of the TPC making use of final refits in the TPC and the ITS. These global tracks, reconstructed from TPC and ITS, are then used to determine the interaction vertex with the best possible resolution. The tracking is then finalised by secondary vertex and cascade decay finding. A more comprehensive description of the tracking procedure can be found in [56].

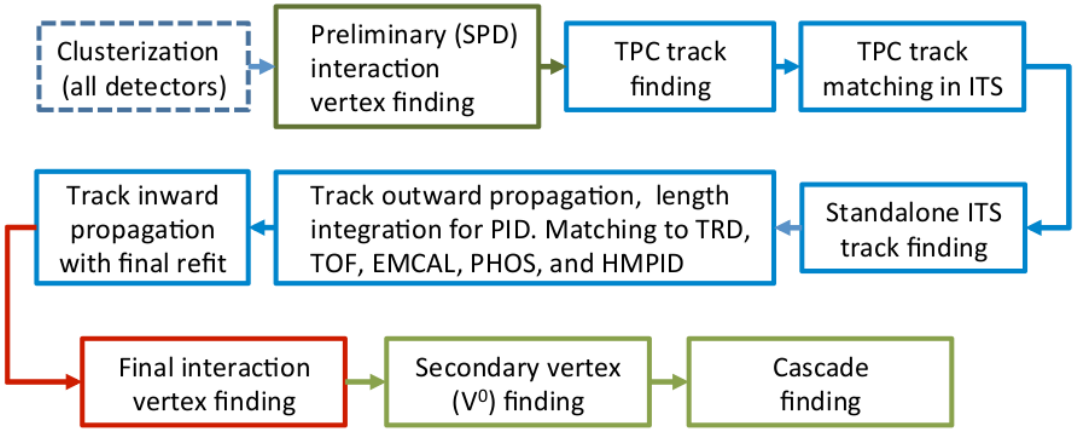

Figure 2.9: Different steps for track reconstruction in the central barrel [56].

After the reconstruction the data are available as Event Summary Data (ESD) which contain for instance information about the tracks and the primary vertex for a given event. A more developed form of data, the Analysis Object Data (AOD), are obtained from a filtering process. They can be filled with tracks that fulfil only certain criteria or already reconstructed jets. How charged jets are reconstructed in ALICE will be discussed in the next section. The ESD and AOD data allow users to do analysis by looping over a large sample of reconstructed events.

2.5 Charged Jet Reconstruction in ALICE

Jet reconstruction and jet measurements are often based on calorimetric information. Since the EMCal has only partial coverage of the ALICE central barrel acceptance and also since in the momentum range of interest for ALICE the tracking detectors still have a suitable momentum resolution a different approach can be used: Jets can be reconstructed only from charged tracks for which the full azimuthal coverage can be exploited.
AliRoot provides an interface to the FastJet [62] package which includes all commonly used jet reconstruction algorithms and other jet analysis tools. In this work jets are reconstructed with the anti-k_T algorithm [63] which is a typical choice in high

energy collider experiments at the LHC. Background estimation is often carried out using the k_{T} algorithm [64], but in this work a different approach is used and will be explained later.

The anti-k_{T} algorithm belongs to the group of sequential recombination algorithms. Those algorithms cluster the tracks according to the distance measures

$$d_{ij} = \min(k_{\mathrm{T}i}^{2p}, k_{\mathrm{T}j}^{2p}) \cdot \frac{\Delta_{ij}^2}{R^2}, \qquad d_{iB} = k_{\mathrm{T}i}^{2p}, \tag{2.1}$$

where $\Delta_{ij}^2 = (\phi_i - \phi_j)^2 + (\eta_i - \eta_j)^2$ is the spatial distance between two entities (particles or pseudojets) i and j, $k_{\mathrm{T}i}$ is the transverse momentum of entity i and p classifies the algorithm ($p = 1$: k_{T}, $p = 0$: Cambridge/Aachen, $p = -1$: anti-k_{T}). The jet radius parameter R is a parameter fixed by the user and it realises an abort criterion for the clustering. For the anti-k_{T} algorithm R can roughly be seen as a geometrical radius, but this will be discussed later in this section.
The clustering starts with a list of entities for a given event. Then the algorithm searches for the smallest of the two distances in 2.1 between two entities and if it is a d_{ij} moves them to a list of pseudojets and continues clustering. If it is a d_{iB} then the entity i (pseudojet or particle) is called a jet and moved to a separate list. The clustering continues until the event no longer contains particles and the list of jets is filled.
Due to the exponent of $p = -1$ jets that are found with the anti-k_{T} algorithm have distinct features. The shape of the jet is less adaptable to soft radiation than for other algorithms and the area is typically circular. Figure 2.10 shows a comparison between the jet areas for the k_{T} and anti-k_{T} algorithm.

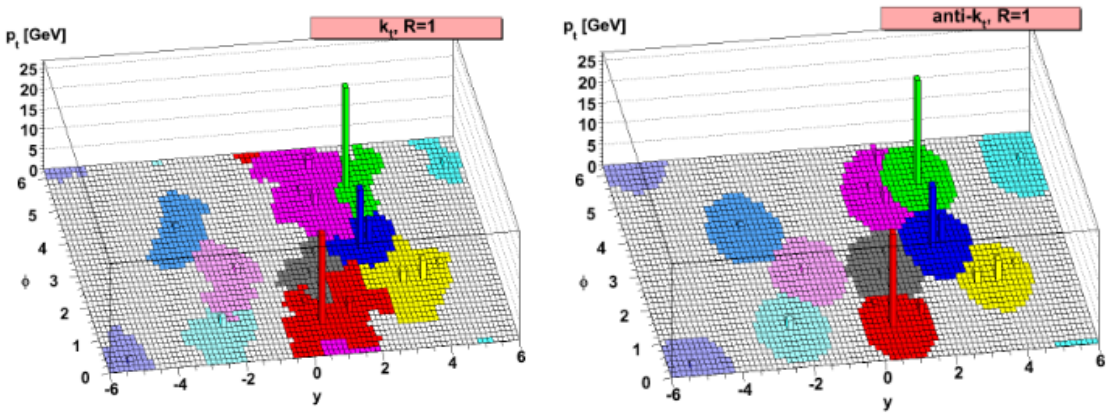

Figure 2.10: Comparison of jet areas for a generated parton level event clustered with the k_{T} and anti-k_{T} algorithm [63].

The area of the jets can be determined with FastJet in different ways. The basics idea is to fill the event with so-called 'ghost' particles with very low momentum

and run the clustering again. The area of a given jet can then be extracted from the ghost particles associated with the jet. A more detailed description of jet area determination can be found in [62; 65].
In ALICE, due to the limited pseudorapidity acceptance, only the transverse momentum of the jets is reconstructed. In this work the boost invariant p_{T} scheme is used which reconstructs the transverse momentum of the jet from the track momenta as $p_{\mathrm{T,\,jet}} = \sum p_{\mathrm{T,\,track}}$. The consistent definition of the ξ variable introduced in Sec. 1.3.1 is then: $\xi = \ln(1/z) = \ln(p_{\mathrm{T,\,jet}}/p_{\mathrm{T,\,track}})$.

3 Charged Jet Fragmentation in p-Pb Collisions

3.1 Analysis Outline

It is the goal of this work to measure the fragmentation of charged jets in p-Pb collisions with minimum bias and TRD triggered data. It is also the goal to show a comparison of this observable for p-Pb and pp collisions.
ALICE has recorded significant amounts of TRD triggered data during pp data taking in 2012 and p-Pb data taking in 2013 (see Table 3.1). While in 2012 pp collisions took place at $\sqrt{s_{\mathrm{NN}}} = 8$ TeV the center-of-mass energy for p-Pb collisions in 2013 was $\sqrt{s_{\mathrm{NN}}} = 5.02$ TeV. Significant amounts of pp minimum bias data were also recorded in 2010 and 2011 for different center-of-mass energies, but in order to assure consistency with the TRD triggered data it was chosen to only use the 2012 pp and 2013 p-Pb minimum bias data for this analysis.

Year	Collision System	$\sqrt{s_{\mathrm{NN}}}$ (TeV)	$\mathrm{N}^{\mathrm{MB}}_{\mathrm{Events}}$ (10^6)	$\mathrm{N}^{\mathrm{HJT}}_{\mathrm{Events}}$ (10^6)
2012	pp	8.0	270	1.56
2013	p-Pb	5.02	134	0.99

Table 3.1: Overview of recorded statistics for 2012-2013 data taking for Minimum Bias (MB) and TRD jet triggered (HJT) data. The numbers for MB refer to the coincident V0 signal (V0AND). Numbers are taken from [66] and [67].

The number of analysed events is reduced by quality assurance (see Sec. 3.2) and event selection. In the event selection events that do not fulfil certain quality criteria are excluded. In Table 3.2 the applied event selection cuts are shown separately for p-Pb minimum bias data taken in periods LHC13bc and LHC13ef due to the different running conditions [68].

Pile-up events are events that contain more than one inelastic (pp or p-Pb) collision. These can occur in the same bunch crossing ('in-bunch pile-up') or from a later bunch crossing if the electronics are still recording ('out-of-bunch pile-up'). Those events can be recognised from multiple reconstructed vertices. In addition using the correlation between the number of clusters and tracklets in the SPD for a given event, the background and pile-up contribution can be reduced further. Both cuts are contained in 'SPD pile-up rejection'. From Table 3.2 it can be seen that the number of accepted event after pile-up rejection is smaller for the later periods LHC13ef. In

Criterion	Accepted events 13bc [%]	Accepted events 13ef [%]
SPD pile-up rejection	99.6	98.2
$N_{\text{Contributors}} \geq 3$	95.0	93.8
$\lvert z_{\text{Vertex}} \rvert \leq 10$ cm	85.0	84.5

Table 3.2: Event selection (dependent cuts) used in this analysis. Numbers are given for p-Pb minimum bias data from periods LHC13bc and LHC13ef separately.

the periods LHC13ef the interaction rate was significantly higher than for LHC13bc [68]. Thus pile-up events are more likely for those periods and the rejection of those has to be higher.
For this analysis the primary vertex is requested to be reconstructed from at least three contributing tracks ($N_{\text{Contributors}}$) to make sure that events have a real primary vertex. Events having vertices with $|z_{\text{Vertex}}| > 10$ cm are excluded to reduce effects arising from the acceptance deterioration.

Charged jets are then reconstructed in the accepted events from tracks with $p_{\text{T, track}} > 0.15$ GeV/c and $|\eta|_{\text{track}} < 0.9$ with the anti-k_{T} algorithm with $R_{\text{jet}} = 0.4$. To the tracks fed to the jetfinder and those used for plotting inclusive track distributions quality cuts are applied consistently. The tracks that are used are required to have an ITS contribution ('refit' from last tracking step) to optimise the momentum resolution and to minimise the contribution of tracks arising from out-of-bunch pile-up events. The jet acceptance is limited geometrically to $|\eta|_{\text{jet}} < |\eta|_{\text{track}} - R_{\text{jet}} = 0.5$.

3.2 Quality Assurance

As mentioned earlier the data that are used in this analysis were recorded in 2012 (pp) and 2013 (p-Pb). These data were taken in different data taking periods in which every period is subdivided into several runs. Table 3.3 shows an overview of the number of analysed events after quality assurance and event selection.

Period	$N^{\text{MB}}_{\text{Events}}$ (10^6)	$N^{\text{HJT}}_{\text{Events}}(10^6)$
LHC12h	26.5	0.7
LHC13b	25.8	0
LHC13c	77.7	0
LHC13e	0	0.2
LHC13f	0	0.3

Table 3.3: Number of analysed events for pp (LHC12h) and p-Pb (LHC13x) data taking periods

For the analysis, runs that have been marked as 'bad' in the run condition table [66] were excluded. In addition a detailed Quality Assurance (QA) was carried out.

For tracks and jets different distributions are monitored run by run and compared to the period average. Runs with non-optimal detector performance are excluded to ensure uniform track acceptance. Jet finding algorithms are very sensitive to gaps in the track acceptance since losses of tracks can lead to a change of the reconstructed jets. Figure 3.1 shows the comparison of the track azimuthal distributions for two runs from LHC13f minimum bias with the period average. The left figure shows a typical good run while the right figure shows a run that was excluded due to non-uniform acceptance. This non-uniformity of the track acceptance can arise if TPC read-out chambers are partly operated at lower gas gain caused by a lower voltage at the anode wires. This leads to a loss of clusters and therefore reduces the tracking efficiency in this regions.
The list of used runs for all periods can be found in App. B.

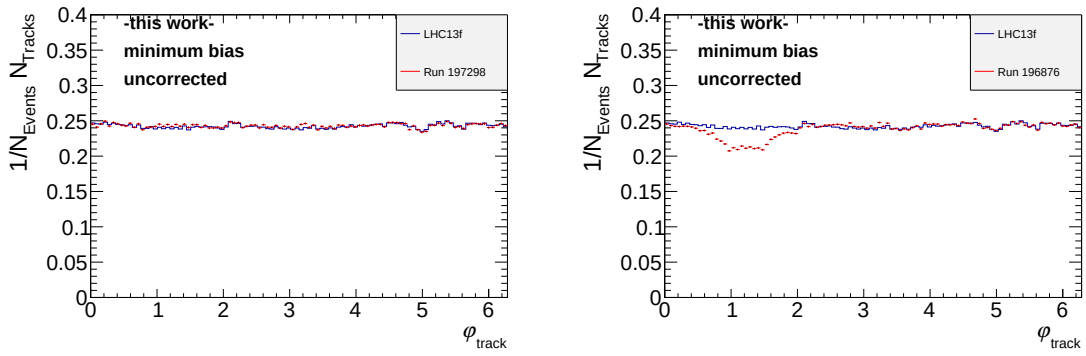

Figure 3.1: Comparison of azimuthal distribution of tracks for runs with period average for LHC13f minimum bias.

3.3 Raw Distributions for p-Pb

In the following minimum bias and TRD triggered data will be compared and the trigger bias discussed. First the minimum bias data will be introduced.

3.3.1 Minimum Bias Data

Since the minimum bias trigger used in this analysis only demands a coincident signal in both V0 scintillators also softer collisions are accepted. Figure 3.2 (left panel) shows the number of tracks that are found in a certain $p_{\mathrm{T,\,track}}$ bin. As can be seen the spectrum is steeply falling which visualises that hard interactions are more unlikely in QCD. The right panel shows the azimuthal distribution for tracks with $p_{\mathrm{T,\,track}} > 3$ GeV/c. The observed structures arise from the acceptance deterioration at the edges of the 18 TPC sectors due to support structures.

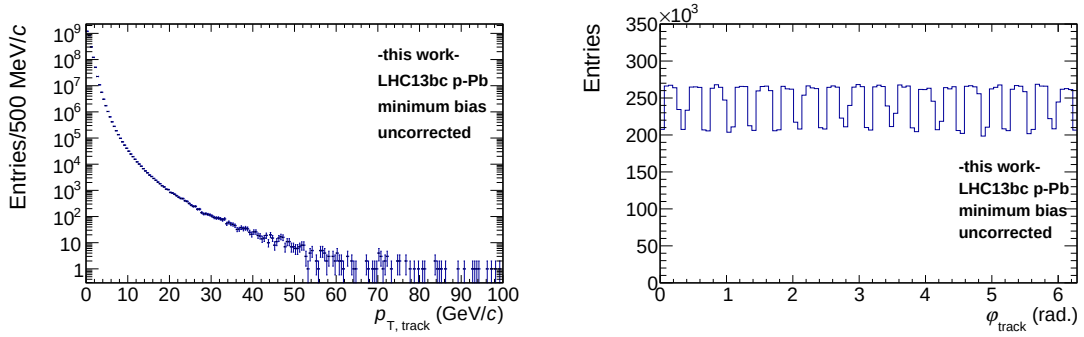

Figure 3.2: Transverse momentum of tracks (left) and azimuthal distribution of tracks with $p_{\mathrm{T,\,track}} > 3$ GeV/c (right)

Since jets are reconstructed from tracks these properties translate also to the jet distributions. Figure 3.3 (left panel) shows the $p_{\mathrm{T,\,jet}}^{\mathrm{raw,\,ch}}$ spectrum. It extends to higher p_{T} than the $p_{\mathrm{T,\,track}}$ spectrum since jets are objects reconstructed from mostly more than one track and the $p_{\mathrm{T,\,jet}}^{\mathrm{raw,\,ch}}$ is the sum of the $p_{\mathrm{T,\,track}}$of the constituents. The azimuthal distribution of jets with $p_{\mathrm{T,\,jet}} > 5$ GeV/c is shown in Fig. 3.3 (right panel). The structures are there less pronounced since jets also contain tracks with low momentum for which the azimuthal distribution is flat as seen in Fig. 3.1.

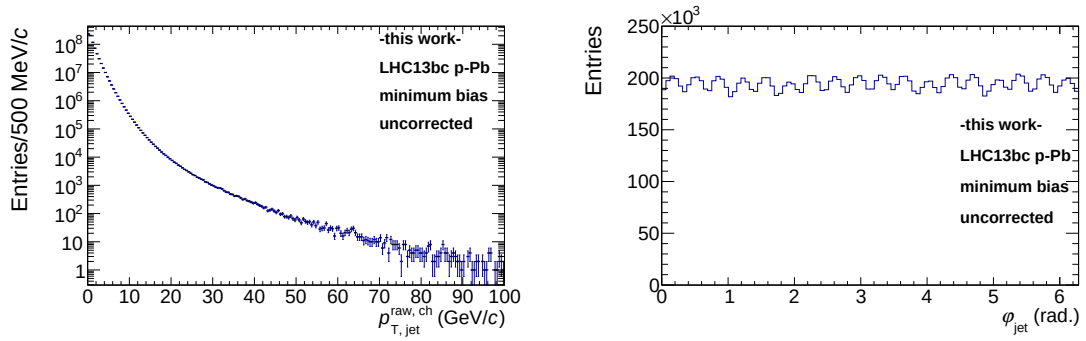

Figure 3.3: Transverse momentum (left) and azimuthal distribution (right) of reconstructed jets. The latter is shown for jets with $p_{\mathrm{T,\,jet}} > 5$ GeV/c

The fragmentation distributions of the jets are then reconstructed from jets in a given $p_{\mathrm{T,\,jet}}$ interval. For this the tracks that are associated with the jet by the jetfinder are used (For clarification: A different approach would be to draw an ideal cone with radius R around the jetaxis and use those tracks that fall into this cone). To study the (longitudinal) momentum distribution of tracks in charged jet we consider the variables $z = p_{\mathrm{T,\,track}}/p_{\mathrm{T,\,jet}}^{\mathrm{raw,\,ch}}$ and $\xi = \ln(1/z)$. Figure 3.4 shows the z and ξ distribution for tracks in jets with 20 GeV/$c \leq p_{\mathrm{T,\,jet}}^{\mathrm{raw,\,ch}} \leq$ 30 GeV/c. Both distributions are normalised to the number of jets in this momentum interval and to the width of the bins. From the z distribution one can see that most tracks carry low momentum fractions of the jet momentum. However, the behaviour at very low $p_{\mathrm{T,\,track}}$ is not visible on a linear scale. Therefore the ξ variable is introduced which shows the logarithm of the inverse of z. Hence low values in ξ translate into large track momenta and high ξ values translate into low track momenta. $\xi = 0$ means $p_{\mathrm{T,\,track}} = p_{\mathrm{T,\,jet}}^{\mathrm{raw,\,ch}}$ (single particle jet) and the highest possible ξ value translates into the lowest possible $p_{\mathrm{T,\,track}}$ value (150 MeV/c). The ξ variable reveals what was only indicated in the z distribution: at very low track momenta the track yield is lower again and most of the tracks actually carry intermediate transverse momenta.

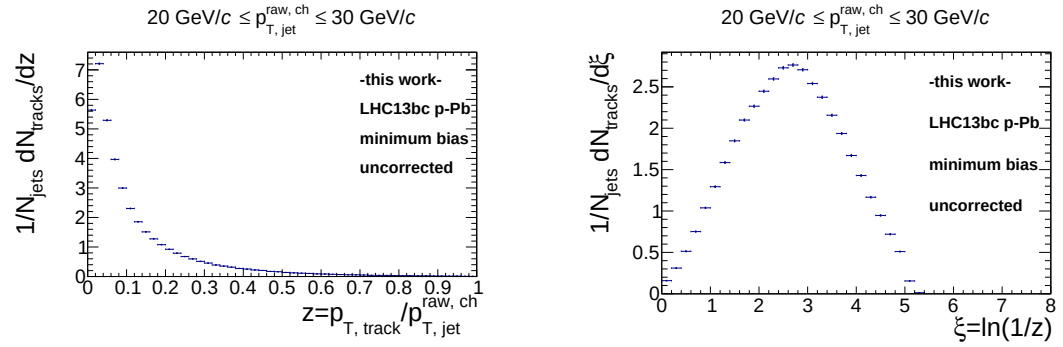

Figure 3.4: z and ξ distribution for tracks in jets reconstructed with raw transverse momentum between 20 GeV/c and 30 GeV/c

3.3.2 TRD Triggered Data

The TRD jet trigger requires three tracks above 3 GeV/c in any TRD stack. Therefore the TRD jet trigger is more restrictive than the minimum bias trigger and will specifically select events that contain high p_{T} tracks or jets respectively. The track spectrum and η distribution is shown in Fig. 3.5. The track φ and $\eta-\varphi$ distributions are shown in Fig. 3.6. All angular distributions are shown again for tracks with $p_{\mathrm{T,\,track}} > 3$ GeV/c.

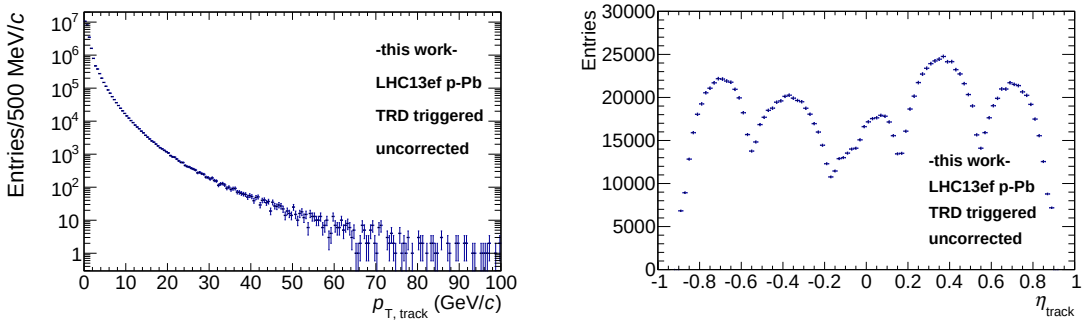

Figure 3.5: Transverse momentum of tracks (left) and pseudorapidity distribution for tracks with $p_{\mathrm{T,\,track}} > 3$ GeV/c (right)

The nonuniform η - φ distribution reflects the TRD trigger acceptance. Events that contain high p_{T} tracks which lie in regions without TRD supermodules (two larger bands in azimuth) or with inactive TRD stacks are not selected. Therefore high p_{T} tracks are concentrated at positions of active TRD stacks. However, a triggered event can also contain tracks above 3 GeV/c in other regions (for instance correlated). Thus the track yield does not vanish in regions without TRD.

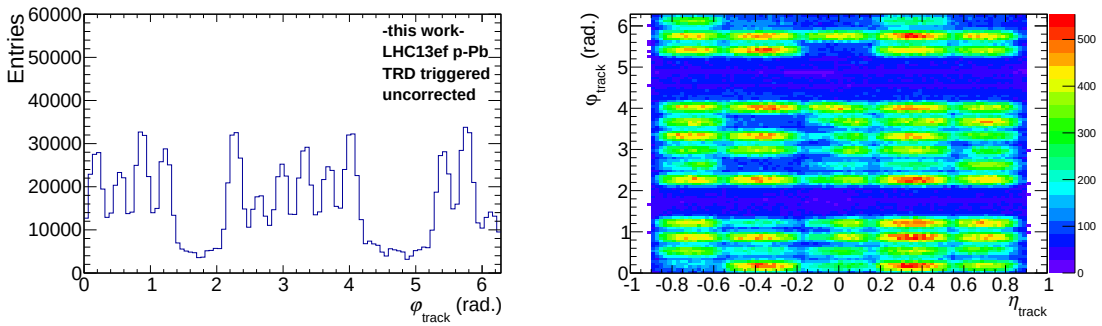

Figure 3.6: Azimuthal distribution of tracks (left) and η-φ map of tracks (right) (Both for tracks with $p_{\mathrm{T,\,track}} > 3$ GeV/c)

The track distributions again translate into fairly similar jet distributions. Figure 3.7 shows the $p_{\mathrm{T,\,jet}}^{\mathrm{raw,\,ch}}$ spectrum and the η_{jet} distribution. The $p_{\mathrm{T,\,jet}}^{\mathrm{raw,\,ch}}$ histogram is filled of course only in those events for that the TRD jet trigger was fired. That means that jets below $3 \cdot 3$ GeV/c $= 9$ GeV/c are mostly jets that have not been triggered on. Around 9 GeV/c the onset of the jet trigger is visible.
The η_{jet} distribution shows a slight asymmetry which is be caused by the asymmetric trigger acceptance (see also Fig. 3.6).

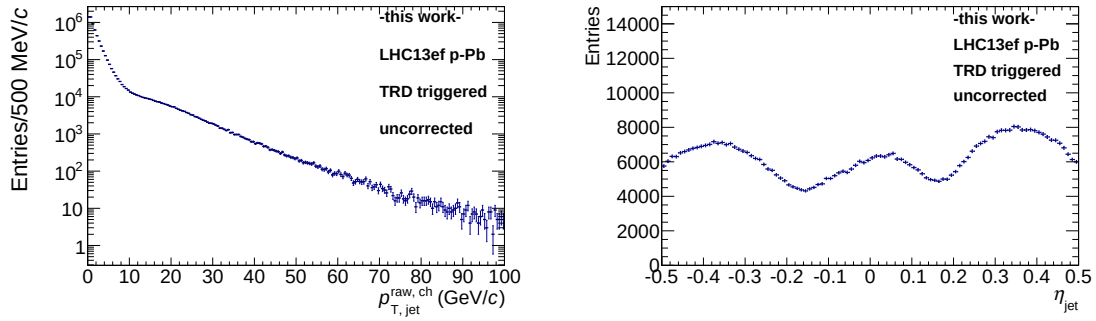

Figure 3.7: Transverse momentum (left) and pseudorapidity distribution (right) of reconstructed jets. The latter is shown for jets with $p_{\mathrm{T,\,jet}}^{\mathrm{raw,\,ch}} > 5$ GeV/c

The fragmentation distributions are constructed in the same way as for minimum bias data. However due to the trigger condition they are biased at lower $p_{\mathrm{T,\,jet}}^{\mathrm{raw,\,ch}}$ (see Fig. 3.8). Events that contain jets which are not reconstructed online with three tracks above 3 GeV/c, but have a softer composition, are rejected. Therefore the track yield below 3 GeV/c is depleted in Fig. 3.8 left.
But for higher jet momenta it will be more and more likely for jets to fulfil the trigger condition. Thus at high enough $p_{\mathrm{T,\,jet}}^{\mathrm{raw,\,ch}}$ the bias will vanish eventually. Figure 3.8 right shows the fragmentation distribution for jets with 80 GeV/$c \leq p_{\mathrm{T,\,jet}}^{\mathrm{raw,\,ch}} \leq 100$ GeV/c. The ξ value that corresponds to a $p_{\mathrm{T,\,track}}$ of 3 GeV/c is shifted since it depends on $p_{\mathrm{T,\,jet}}^{\mathrm{raw,\,ch}}$. In this plot no bias is visible which suggests to use the fragmentation distributions of the triggered data above 80 GeV/c. In [60] fragmentation distributions for TRD and EMCal triggered data are compared for pp collisions for the bin 80 to 100 GeV/c and show a good overall agreement. For intermediate ξ values the agreement is better than ≈ 6 % which makes us confident that the residual bias is small. A possible way to quantifiy this residual bias will be discussed in Chapter 5.

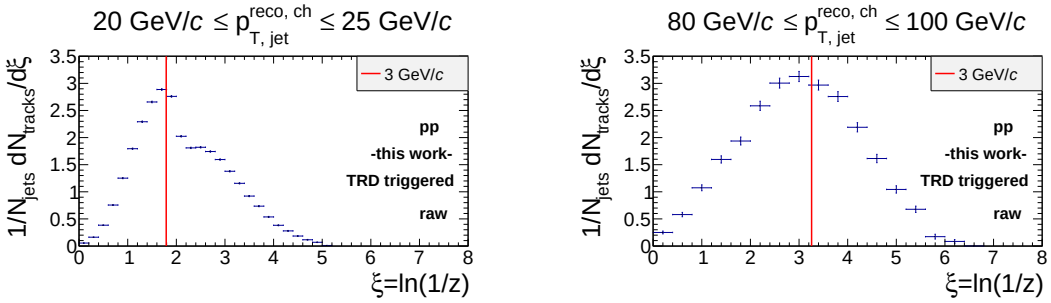

Figure 3.8: Fragmentation distributions for jets in TRD triggered data. At lower $p_{\mathrm{T,\,jet}}^{\mathrm{raw,\,ch}}$ (left plot) a bias below 3 GeV/c can be seen. For jets with $p_{\mathrm{T,\,jet}}^{\mathrm{raw,\,ch}} > 80$ GeV/c (right plot) no bias can be seen.

3.4 Underlying Event Study

The comparison of the fragmentation distributions for different collision systems requires the subtraction of the underlying event which is different among those.

3.4.1 Definition

The underlying event is the track activity in the event which is uncorrelated to the hard scattering. Experimentally there is no unique definition of the underlying event. Different approaches are used among different analyses in ALICE in order to quantify the underlying event. For Pb-Pb analyses a technique is used in which the event is clustered a second time with the $\mathrm{k_T}$ algorithm. An averaging procedure over the found jets determines the average underlying event p_{T} density which is then subtracted event-by-event from the p_{T} of the signal jets that are found with the anti-$\mathrm{k_T}$ algorithm [69], [70].
For p-Pb collisions this procedure is not naively applicable. Due to the lower multiplicity density in p-Pb collisions compared to (central) Pb-Pb collisions the approach has to be modified. A scaling factor has to be introduced to account for regions where no particles or jets are found [46].
In this work a simpler approach will be used: In every event the leading jet (jet with highest $p_{\mathrm{T,\,jet}}$) is found and two cones are placed at the same η and $\Delta\varphi = \pm\pi/2$ (perpendicular cones, see Fig. 3.9). These cones have the same radius R as the jet resolution parameter. Tracks that fall into these cones are then used for the estimation of the underlying event. The motivation for the placement of these cones is to maximise the distance from a back-to-back dijet pair in azimuth. The η placement accounts for the pseudorapidity dependence of the underlying event.

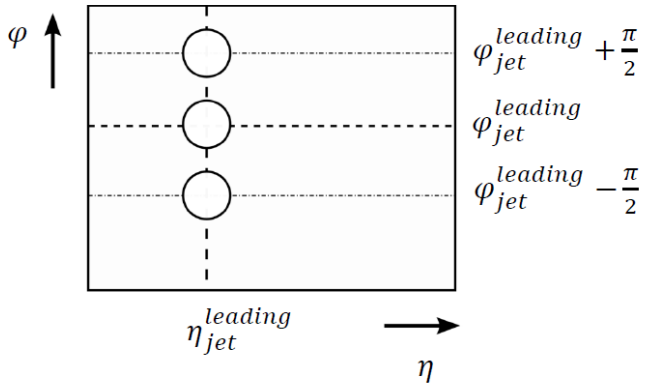

Figure 3.9: Visualisation of detector acceptance (η - φ) and schematic placement of perpendicular cones with respect to leading jet

3.4.2 Properties of Underlying Event

The transverse momentum density ρ and the number of tracks in the underlying event are estimated with these perpendicular cones in p-Pb and pp collisions. The transverse momentum density is defined as

$$\rho = \text{mean}\left(\frac{p_{\mathrm{T}}^{i}}{\mathrm{A}^{i}}\right), \qquad \text{i=1,2 perp. cones,} \tag{3.1}$$

where p_{T}^{i} is the transverse momentum found in cone i and $\mathrm{A}^{i} = \pi R^2$ is its area. The ρ can be calculated in every event and then used for underlying event subtraction (see next section). In order to illustrate the magnitude of the transverse momentum density Fig. 3.10 shows the average for one data taking period. To reveal possible correlations to jet production it is plotted versus the raw transverse momentum of the leading jet $p_{\mathrm{T,\,jet}}^{\mathrm{leading,\,raw}}$.

Figure 3.10 also shows the number of tracks in the underlying event for pp and p-Pb collisions. For both observables no significant correlation to $p_{\mathrm{T,\,jet}}^{\mathrm{leading,\,raw}}$ is found. Between the underlying event in p-Pb and pp a constant scaling factor (≈ 2) is observed.

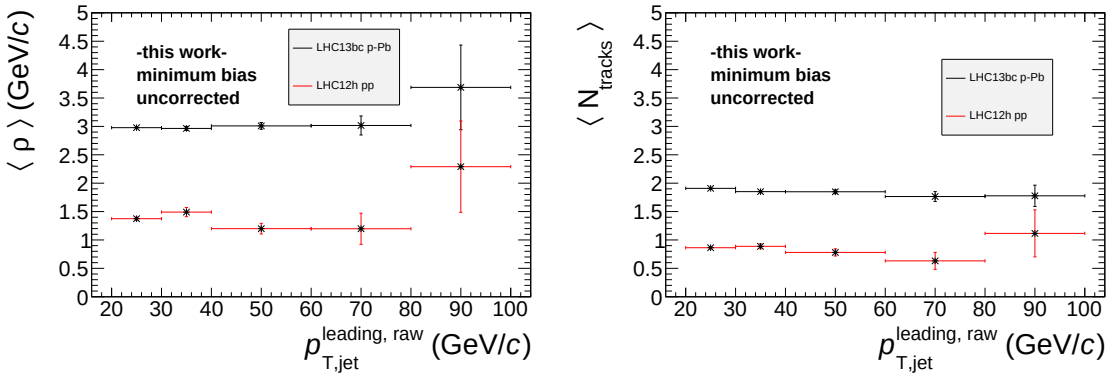

Figure 3.10: Average underlying event p_{T} density (left) and average number of tracks found in perpendicular cones (right). Here p-Pb collisions at 5.02 TeV and pp collisions at 8 TeV are compared. No corrections for detector effects are applied.

3.4.3 Subtraction

In this section the subtraction procedure for the underlying event will be explained. The underlying event has in principle two major contributions to the fragmentation distributions: It increases the transverse momentum of the reconstructed jets and it contributes to fragmentation distribution. Both contributions will be subtracted as explained in the following.

The p_{T} contribution is subtracted event-by-event from all signal jets using the following scheme which accounts for the jet area:

$$p_{\mathrm{T,\ jet}}^{\mathrm{reco},j} = p_{\mathrm{T,\ jet}}^{\mathrm{raw},j} - \rho \cdot A_{\mathrm{jet}}^{j}, \qquad \text{j=1,2,...,n jets.} \tag{3.2}$$

The second contribution can be estimated by calculating the fragmentation distribution of the tracks in the perpendicular cone using the transverse momenta of the jets in the event:

$$\xi = \ln \frac{p_{\mathrm{T,\ jet}}^{\mathrm{reco},j}}{p_{\mathrm{T,\ track}}^{\mathrm{perp.\ cone}}}. \tag{3.3}$$

Figure 3.11 shows this contribution for p-Pb and also a comparison of this contribution to pp is shown. The contribution is found to be larger for p-Pb which is consistent with previous observations for the underlying event.

This contribution is finally subtracted on the event ensemble level using the following scheme:

$$dN/d\xi^{\mathrm{jet,\ sub}} = dN/d\xi^{\mathrm{jet}} - \frac{\langle A_{\mathrm{jet}} \rangle}{\pi R_{\mathrm{jet}}^2} \cdot dN/d\xi^{\mathrm{perp.\ cone}}. \tag{3.4}$$

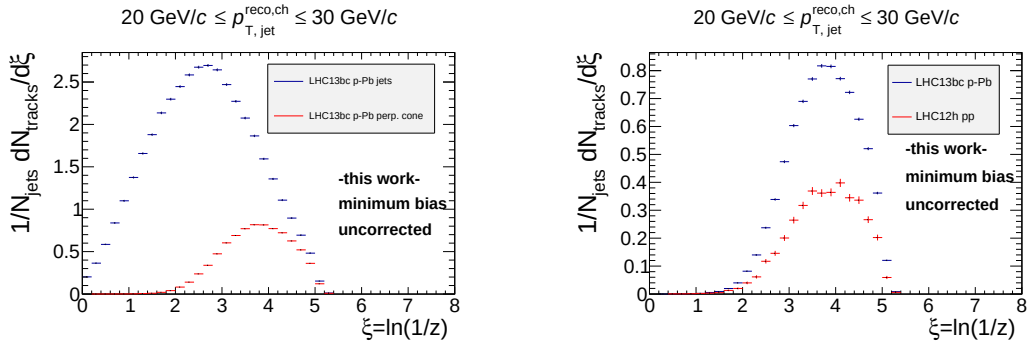

Figure 3.11: Jet fragmentation distribution for p-Pb with contribution from perpendicular cones (left) and comparison of perpendicular cone contribution for pp collisions at 8 TeV and p-Pb collisions at 5.02 TeV. No corrections for detector effects are applied.

The scaling factor in the second term accounts for the non-equal areas of jets and perpendicular cones.

3.5 Comparison of pp and p-Pb Fragmentation Distributions

In this section we compare the fragmentation distributions for pp and p-Pb in bins of the underlying event subtracted transverse momentum $p_{\mathrm{T,\,jet}}^{\mathrm{reco,\,ch}}$. Ideally they are on average compared for the same parton p_{T} in this way. At this stage the distributions are not yet corrected for detector effects. This will be discussed in Sec. 3.6.
First, we focus on the comparison at low $p_{\mathrm{T,\,jet}}^{\mathrm{reco,\,ch}}$ for minimum bias data.

Minimum bias data

The comparison between the fragmentation distributions for p-Pb and pp is shown for $p_{\mathrm{T,\,jet}}^{\mathrm{reco,\,ch}} > 20$ GeV/c to avoid a significant contribution from 'fake jets'. These are low $p_{\mathrm{T,\,jet}}^{\mathrm{reco,\,ch}}$ jets that are clustered from underlying event tracks.
Figure 3.12 shows the two lowest $p_{\mathrm{T,\,jet}}^{\mathrm{reco,\,ch}}$ bins. For both bins a slight enhancement is observed for intermediate to high ξ values.

There are different possible causes for this effect. A residual contamination from fake jets could bias the observed fragmentation since these would show a softer fragmentation pattern than real jets. Due to the higher multiplicity in p-Pb this effect would be of course stronger in p-Pb, thus enhancing the p-Pb distribution. Different effects could arise from the different center-of-mass energies for which the data of both collision systems have been recorded. The jet spectra for both energies show a slightly different shape which causes the mean of the $p_{\mathrm{T,\,jet}}^{\mathrm{reco,\,ch}}$ for a given bin to be different for both collision systems. Since the dependence of the ξ variable on $p_{\mathrm{T,\,jet}}^{\mathrm{reco,\,ch}}$ is logarithmic it is stronger for small $p_{\mathrm{T,\,jet}}^{\mathrm{reco,\,ch}}$. Thus this effect would manifest

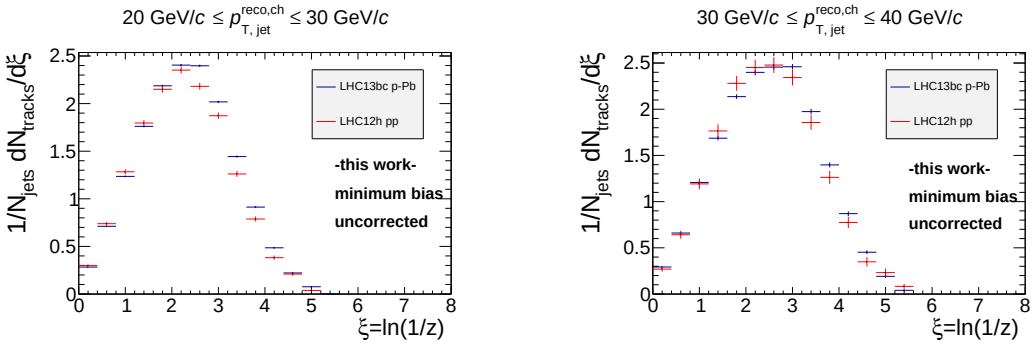

Figure 3.12: Comparison of fragmentation distributions for pp 8 TeV and p-Pb 5.02 TeV minimum bias data for the bins 20 GeV/c to 30 GeV/c (left) and 30 GeV/c to 40 GeV/c (right). No corrections for detector effects are applied.

itself at lower $p_{\mathrm{T,\,jet}}^{\mathrm{reco,\,ch}}$, if at all. Also, due to the different center-of-mass energies different regions of the parton distribution functions are probed for a given produced parton momentum. This could modify the ratio of produced quarks and gluons which fragment differently, thus leading to a deviation for the observed fragmentation distributions. Lastly, these distributions are not corrected for detector effects and shown without systematic uncertainty. Different tracking efficiencies for these data would have an influence on the fragmentation distributions. Sources of systematic uncertainties are discussed in section 4.
For the next higher bins which are shown in Fig. 3.13 no significant deviation between both collision systems is found.

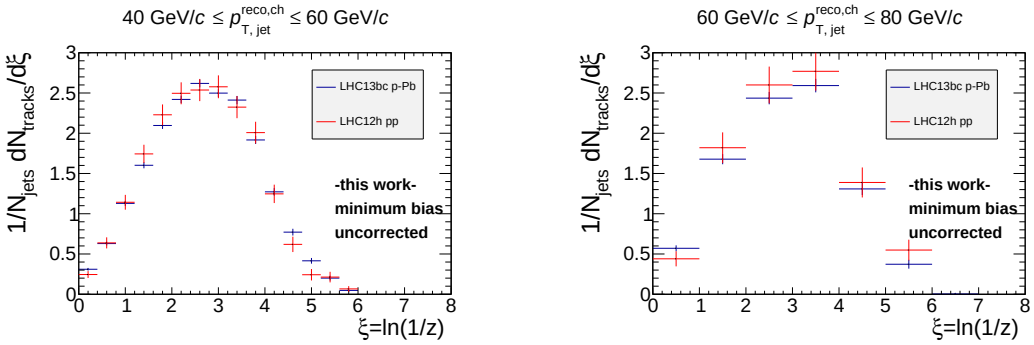

Figure 3.13: Comparison of fragmentation distributions for pp 8 TeV and p-Pb 5.02 TeV minimum bias data for the bins 40 GeV/c to 60 GeV/c (left) and 60 GeV/c to 80 GeV/c (right). No corrections for detector effects are applied.

As mentioned earlier the minimum bias data is clearly limited in terms of statistics. We consider the 60 GeV/c to 80 GeV/c bin the last bin with enough statistics. To extend the range of the measurement we will use TRD triggered data for bins with

higher $p_{\mathrm{T,\,jet}}^{\mathrm{reco,\,ch}}$.

TRD triggered data

In Fig. 3.8 we showed that above $p_{\mathrm{T,\,jet}}^{\mathrm{reco,\,ch}} > 80$ GeV/c the TRD triggered data show no visible bias. Therefore we will use these data above $p_{\mathrm{T,\,jet}}^{\mathrm{reco,\,ch}} > 80$ GeV/c. In Fig. 3.14 three transverse momentum bins are shown. In all bins a good overall agreement between pp and p-Pb is found.

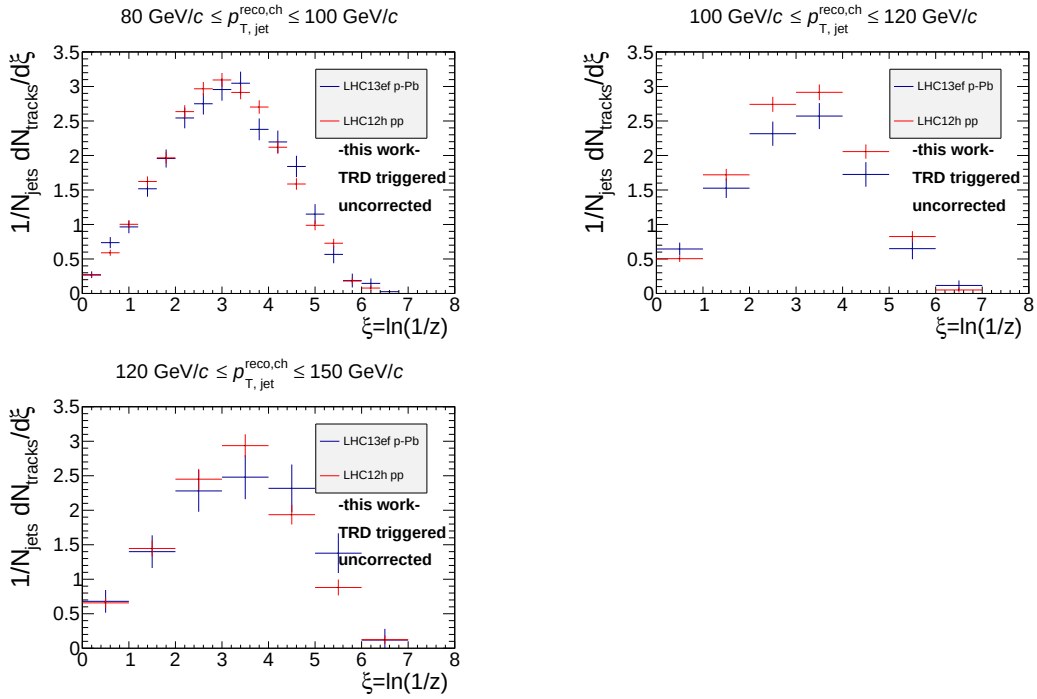

Figure 3.14: Comparison of fragmentation distributions for pp 8 TeV and p-Pb 5.02 TeV TRD triggered data for the bins 80 GeV/c to 100 GeV/c (upper left), 100 GeV/c to 120 GeV/c (upper right) and 120 GeV/c to 150 GeV/c (lower left). No corrections for detector effects are applied.

The fragmentation distributions have to be corrected for detector effects like inefficiencies and momentum resolution. For this, correction factors are derived from a Monte Carlo simulation. These will be discussed in the next section.

3.6 Correction to Hadron Level

At the time the analysis was carried out a full jet Monte Carlo simulation was only available for a center of mass energy of 5.02 TeV for pp collisions. But since it was found that the tracking efficiency in the ALICE central barrel does not depend on the detector occupancy [56] we will use this simulation for the correction of the p-Pb fragmentation distributions.
In the simulation jet events are generated with PYTHIA 6 [22] Tune Perugia 2011 [71] and propagated through the ALICE detector with GEANT3 [72]. Since highly energetic jets are very rare in minimum bias productions it would be too time consuming to generate enough statistics. Instead, each event is forced to contain hard partons with transverse momentum $p_{\mathrm{T}}^{\mathrm{hard}}$ in a given interval ('$p_{\mathrm{T}}^{\mathrm{hard}}$ bin'). Typically ten samples of complementary $p_{\mathrm{T}}^{\mathrm{hard}}$ bins, covering in total a range between a lower cutoff of 5 GeV/c and about 300 GeV/c, are produced with roughly the same number of generated events. The lower cutoff is well below the lowest jet p_{T} bin used in this analysis (20 - 30 GeV/c). The analysis is run over all the $p_{\mathrm{T}}^{\mathrm{hard}}$ bins separately. To obtain a physically meaningful jet spectrum from the different $p_{\mathrm{T}}^{\mathrm{hard}}$ bins they have to be added with different weighting factors that account for the lower probability to produce high p_{T} jets. The weighting of the different bins is carried out according to the following scheme:

$$dN/dp_{\mathrm{T}} = \sum_i \frac{\sigma_i}{N^i_{\mathrm{trials}}} \cdot dN^i/dp_{\mathrm{T}}, \tag{3.5}$$

where i denotes bin i, σ_i is the total partonic production cross section for the events in this bin and N^i_{trials} is the number of generated events. Figure 3.15 shows the fraction of events that are generated with a given $p_{\mathrm{T}}^{\mathrm{hard}}$ after unweighted merging (left) and after the merging according to 3.5 (right).

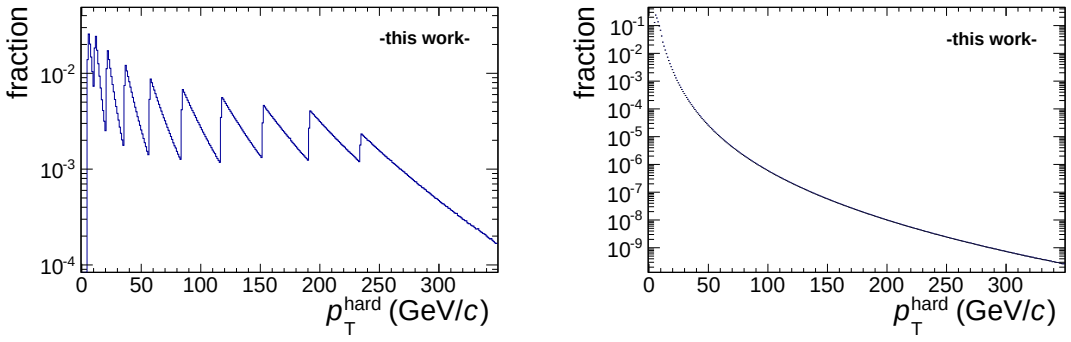

Figure 3.15: Generated event fraction for a given $p_{\mathrm{T}}^{\mathrm{hard}}$ after unscaled merging (left) and scaled merging (right) for 5.02 TeV Pythia Perugia 2011.

The unweighted merged sample shows a structure that is caused by the different

$p_{\mathrm{T}}^{\mathrm{hard}}$ bins. The spectrum in each bin is steeply falling which causes the edges between different bins. After weighted merging the parton $p_{\mathrm{T}}^{\mathrm{hard}}$ spectrum has a physically meaningful shape. The simulation can then be used to correct the data for instrumental effects. In the next section the influence of these effects on the jet reconstruction will be discussed.

3.6.1 Influence of Detector Effects on Reconstructed Jets

Detector effects have an influence on the reconstructed jets. The momentum resolution of the individual tracks leads to a smearing of the jet momentum. Detector inefficiencies can lead to losses of tracks which cause a reduction of the reconstructed jet momentum with respect to the 'true' jet momentum. If a high-z fragment of the jet is lost the reduction of jet momentum can be significant and lead to bin migration. This means that a jet which is produced in a given momentum bin is reconstructed with a lower momentum and thus contributes to the fragmentation distribution of jets in a lower momentum bin.
This tracking efficiency can be quantified with the detector simulation and is shown in Fig. 3.16. It is derived from the ratio of generated particles to reconstructed tracks using the generated momentum. Thus it shows the p_{T}-dependent probability to reconstruct a generated particle in the ALICE central barrel for this set of track cuts. The overall tracking efficiency shows a small dependence on transverse momentum. The shape of the efficiency above 1-2 GeV/c is caused by a p_{T}-dependent loss of TPC clusters in the projection of the tracks to dead areas [56].

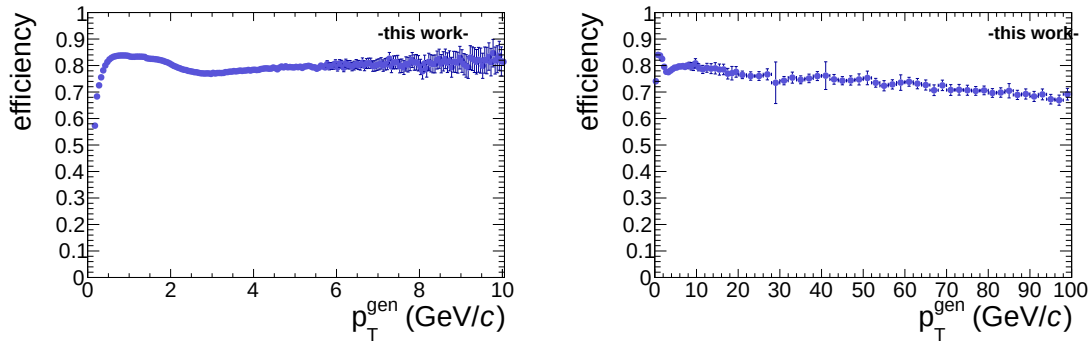

Figure 3.16: Tracking efficiency for particles with generated $p_{\mathrm{T}}^{\mathrm{gen}}$ from 0.15 to 10 GeV/c (left) and 0.15 to 100 GeV/c (right.)

The Monte Carlo simulation also offers the possibility to study jets at particle level. Particle level refers to the state of generated particles before propagation through the detector. After propagation the state is denoted detector level. At particle level the jet reconstruction is applied to generated charged particles. These are required to be physical primaries which means that secondaries from weak decays

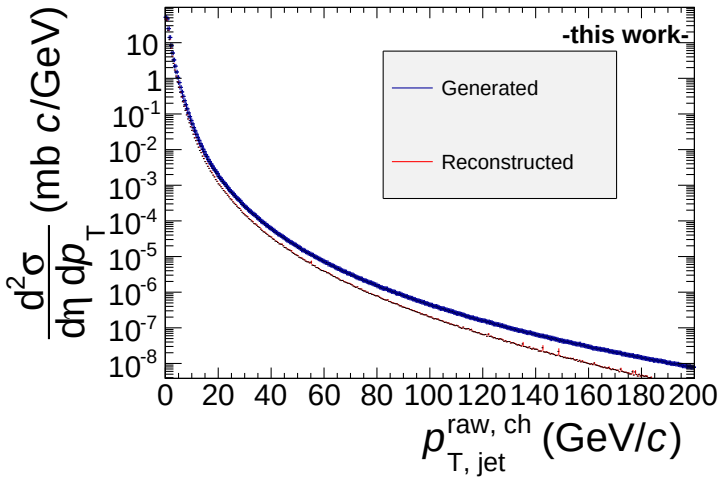

Figure 3.17: Jet cross section for particle level jets ('Generated') and reconstructed detector level jets ('Reconstructed').

are neglected at this stage. The $p_{\mathrm{T,\,particle}} > 0.15$ GeV/c and $|\eta|^{\mathrm{particle}} < 0.9$ cuts are applied consistently to the jetfinding at particle and detector level. At detector level the jet finding is applied to all tracks that are left after kinematic and quality cuts.

Figure 3.17 shows the generated and reconstructed jet cross section for the Monte Carlo simulation. It can be seen that the reconstructed spectrum is systematically shifted to lower $p_{\mathrm{T,\,jet}}^{\mathrm{raw,\,ch}}$ which is due to efficiency losses. From the information on particle and detector level jets we can deduce the correction factors that have to be applied to the measured fragmentation distributions. In the next section we discuss the derivation of those.

3.6.2 Derivation of Correction Factors

The measured fragmentation distributions have to be corrected for detector effects and contamination from secondary particles. The approach used in this analysis is the bin-by-bin correction method. This was already used in [73] to correct the fragmentation distributions for pp collisions. It is based on ratios of observables that are obtained at particle level and those at detector level as a function of the variable x (potentially multi-dimensional). The corrected observable $O_{\mathrm{data}}^{\mathrm{corrected}}(x)$ is then obtained as:

$$O_{\mathrm{data}}^{\mathrm{corrected}}(x) = O_{\mathrm{data}}^{\mathrm{uncorrected}}(x) \cdot \frac{O_{\mathrm{mc}}^{\mathrm{part}}(x)}{O_{\mathrm{mc}}^{\mathrm{det}}(x)}, \tag{3.6}$$

in which $O_{\mathrm{mc}}^{\mathrm{part}}(x)$ is the observable at particle level and $O_{\mathrm{mc}}^{\mathrm{det}}(x)$ is the observable at detector level. Their ratio represents the correction factor that is applied to the

uncorrected observable obtained from data $O_{\text{data}}^{\text{uncorrected}}(x)$.
In our case the observable O and the variables x are given by $O = 1/N_{\text{jets}}\ dN_{\text{tracks}}/d\xi$ and $x = (p_{\text{T, jet}}, p_{\text{T, track}})$. The fragmentation distributions are reconstructed from charged particles in particle and detector level jets as described earlier. The underlying event is subtracted on particle and detector level and the fragmentation distributions are plotted in bins of the $p_{\text{T, jet}}^{\text{reco, ch}}$ that is obtained at particle and detector level. In this way the correction accounts for the reduction of the jet energy scale through efficiency losses and also for momentum resolution of individual tracks. Since the jet reconstruction on particle level is applied to primary particles only we implicitly correct for the contribution of secondary particles. Figure 3.18 (left) shows the fragmentation distribution obtained at particle level ('Generated') and the one obtained at detector level ('Reconstructed') for the $p_{\text{T, jet}}^{\text{reco, ch}}$ bin 40 GeV/c to 60 GeV/c. On the right side of Fig. 3.18 the ratio of the particle level and detector level distribution is shown. It corresponds to the correction factor introduced in Eq. 3.6 for this bin. All plots of correction factors can be found in App. A.

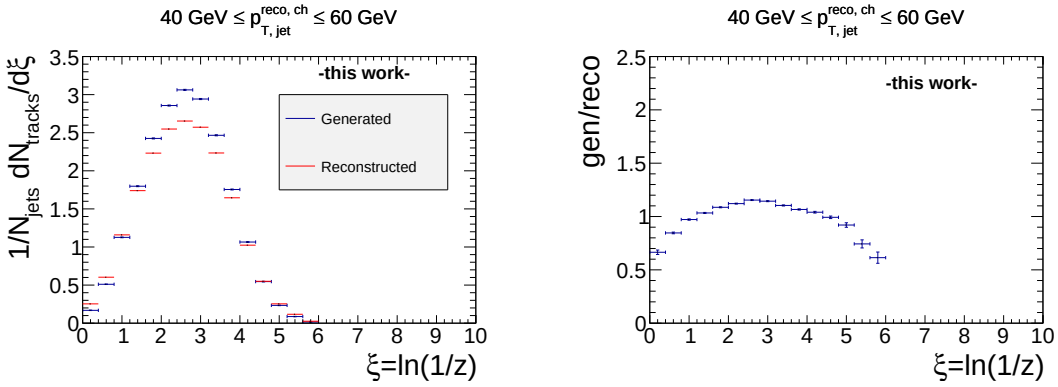

Figure 3.18: Reconstructed fragmentation distributions for jets at particle and detector level (left) and ratio of those (right)

One can see that the correction factors are of the order of 1 which shows that the correction is small. We also observe that at low and high ξ values more tracks are reconstructed than generated. For low ξ values this is due to the reduction of the jet energy. If a high-z particle of a jet is not reconstructed the reconstructed jet momentum will be significantly lower than the generated momentum. Thus, a particle with a given generated $z^{\text{gen}} = p_{\text{T, particle}}^{\text{gen}}/p_{\text{T, jet}}^{\text{gen}}$ will be reconstructed with a significantly higher $z^{\text{reco}} = p_{\text{T, particle}}^{\text{reco}}/p_{\text{T, jet}}^{\text{reco}}$ due to the reduction of the jet momentum. In [73] the correction for secondary particles was carried out separately to the bin-by-bin correction. There the correction factors for the secondary contamination show a similar shape as the bin-by-bin correction factors in this analysis at high ξ values. This suggests that the shape of the correction factors at high ξ values is due to the secondary correction.
In order to assure self-consistency of the correction factors we carried out a closure test which will be described in the next section.

3.6.3 Closure

A closure test is a validation of the correction procedure. We apply the correction factors to the detector level distributions and compare them to the particle level distributions. To avoid autocorrelations the simulation data is subdivided into two statistically independent subsamples. The correction factors are derived from the first sample and then applied to the detector level distributions of the second sample. These are then compared to the particle level distributions of the second sample. Figures 3.19 and 3.20 show this comparison for all $p_{\mathrm{T,\,jet}}^{\mathrm{reco,\,ch}}$ bins together with the ratio of both distributions. The ratios are fitted with a constant to quantify the agreement. In most bins the fit parameter agrees with unity within uncertainties. Using a fully autocorrelated sample we verified that the observed non-closure on a 1 % level in some bins is due to statistical fluctuations. We therefore consider the closure test successful and do not assign a systematic uncertainty. In the next section other potential origins of systematic uncertainties and their estimation will be discussed.

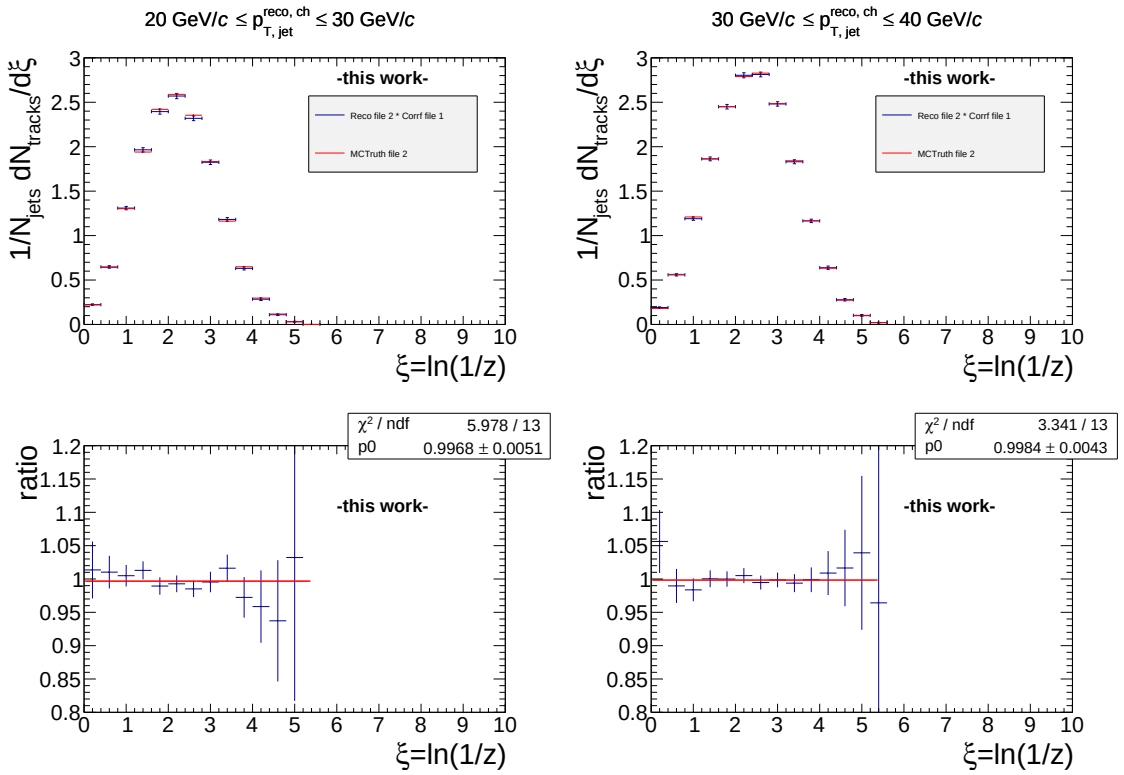

Figure 3.19: Closure test for correction procedure for bins from 20 GeV/c to 40 GeV/c

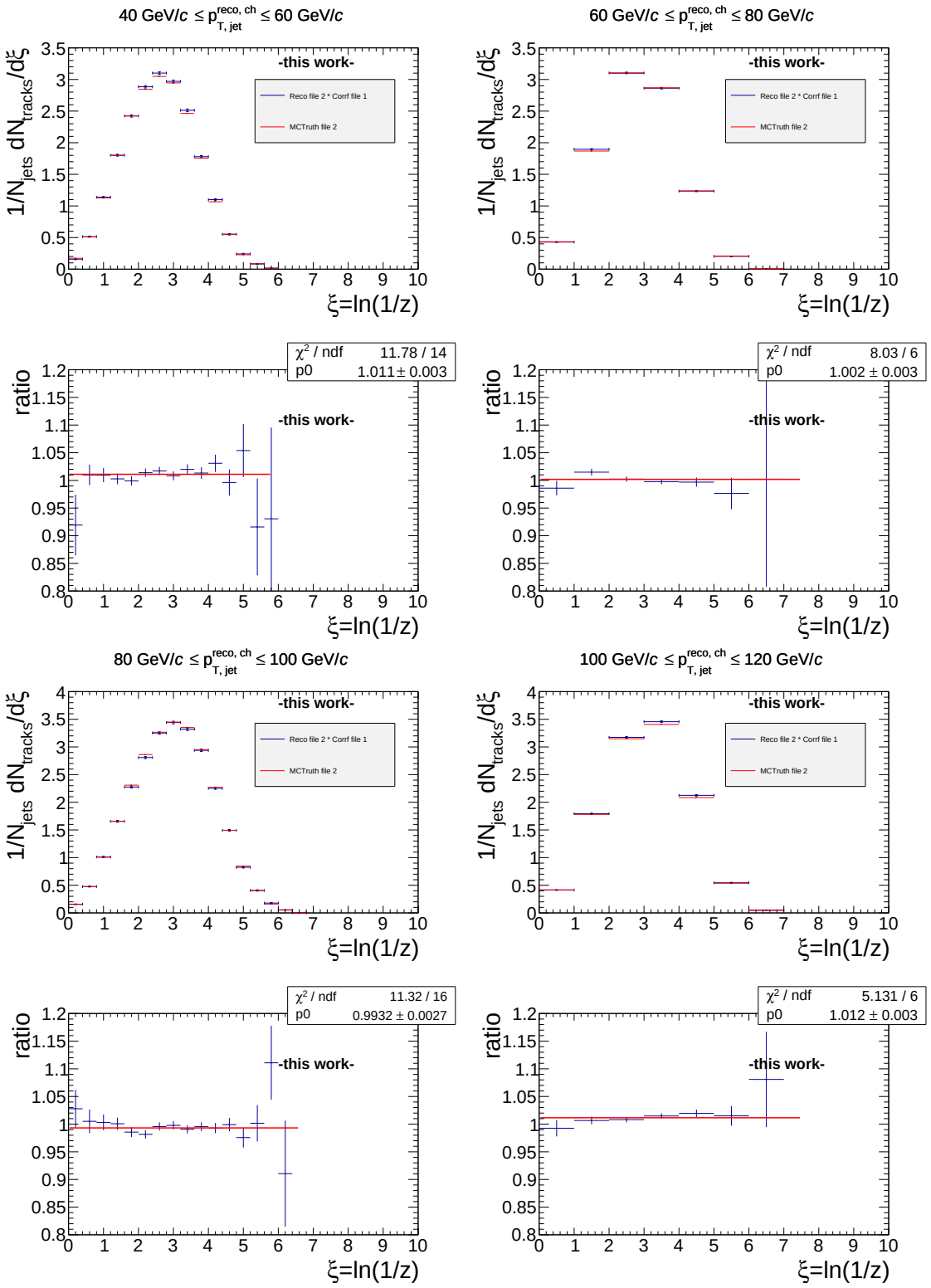

Figure 3.20: Closure test for correction procedure for bins from 40 GeV/c to 120 GeV/c

4 Results

In this chapter we discuss systematic uncertainties and present the final results.

4.1 Estimation of Systematic Uncertainties

4.1.1 Underlying Event Subtraction

The underlying event are particles that are uncorrelated to the hard scattering which is correlated to the jet. Experimentally there is no unique definition of the underlying event and different methods can be used to estimate it. These different methods might yield different results for the underlying event, thus giving rise to a systematic uncertainty. In this analysis we use two perpendicular cones placed relative to the leading jet to estimate the transverse momentum density and the track spectra of the underlying event. These cones reproduce the $\mathrm{dN/d}\eta$ distribution of the leading jet. For subleading jets which exist in ≈ 10 % of all events this is not the case. Furthermore, these cones might overlap with other possible hard jets that are present due to the collision system (average number of nucleon nucleon collisions per p-Pb collision: $\langle N_{\mathrm{coll}} \rangle \approx 7$ [74]).
To estimate the systematic uncertainty of the underlying event subtraction we propose a different method in which a cone of R = 0.4 is placed randomly in the event. This cone is only evaluated in jet events and is only accepted if there is no overlap with a jet above a momentum threshold $p_{\mathrm{T,\,thresh}}$. To not bias the event sample this cone is placed randomly in the event until there is no overlap with those jets. The parameter $p_{\mathrm{T,\,thresh}}$ is in principle a free parameter that can be varied. Since for the perpendicular cones no such veto is introduced, a low cutoff of $p_{\mathrm{T,\,thresh}} = 5$ GeV/c was chosen to maximise the difference of both methods. Per definition these randomly placed cones do not overlap with hard jets, but they might veto also upward fluctuations of the underlying event, thus leading to an underestimation of the underlying event.
For the randomly placed cone we carry out the underlying event subtraction procedure consistently. The obtained fragmentation distributions from both methods are then compared at detector level for the lowest jet p_{T} bin to minimise the influence of statistical fluctuations (see Fig. 4.1 left panel).

The deviation of both methods can be separated into two parts: The deviation at low ξ values and the deviation at intermediate to high ξ values. Due to the veto on jets with $p_{\mathrm{T,\,jet}}^{\mathrm{raw,\,ch}} > 5$ GeV/c the underlying event estimated with the randomly placed cone is on average smaller than the one estimated with perpendicular cones. Thus the fragmentation distribution after subtraction of the underlying event has

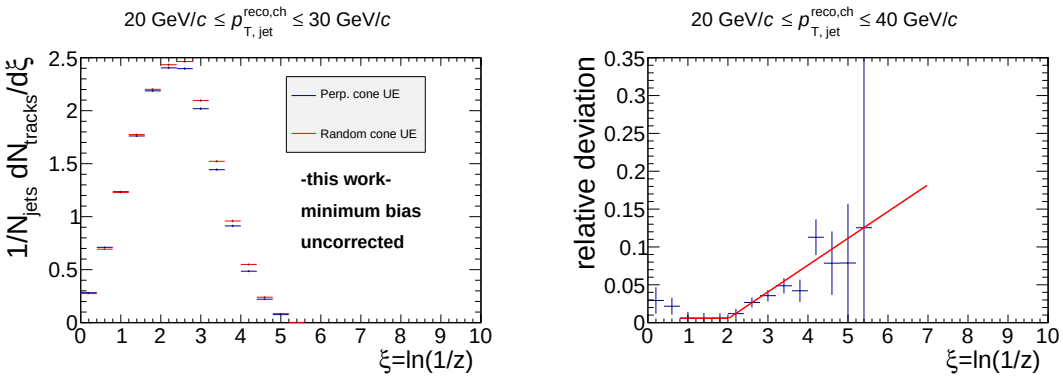

Figure 4.1: Comparison of fragmentation distributions subtracted with underlying event estimated with perpendicular cones and a randomly placed cone (left panel). The right panel shows the relative deviation of both distributions. The red line indicates the section-wise fit of the deviation.

a higher contribution at intermediate to high ξ values in Fig. 4.1. Figure 4.1 right panel shows the relative deviation of both methods. The uncertainty at low ξ values arises from the track p_{T} spectrum in the randomly placed cones. Due to the veto on jets with $p_{\mathrm{T,\,jet}}^{\mathrm{raw,\,ch}} > 5$ GeV/c it has an abrupt cutoff at $p_{\mathrm{T,\,track}} = 5$ GeV/c which corresponds to a ξ value of ≈ 0.6 in the shown bin. We consider this behaviour an overestimation of the uncertainty and we leave this region out in the following.

Since the underlying event p_{T} is on average smaller in the randomly placed cone the transverse momentum $p_{\mathrm{T,\,jet}}^{\mathrm{reco,\,ch}}$ of a given jet after underlying event subtraction is on average higher for this method. Thus the fragmentation distribution of the random cone method is slightly shifted to higher ξ values. This effect is estimated with a fit with a constant in the ξ range 0.8 to 2 and found to be 0.7 %. The deviation at the higher ξ values is estimated with a linear fit. To apply this uncertainty also to higher jet p_{T} bins we apply a linear transformation to the fit function which is derived from jet p_{T} scaling in the ξ variable. The assigned uncertainty is then derived from the fit function if the function is larger than 0.7 %, and 0.7 % elsewhere.

4.1.2 Tracking Efficiency and Momentum Resolution

Systematic uncertainties of the tracking efficiency and momentum resolution of individual tracks lead to a systematic uncertainty of the fragmentation distributions. They arise from the detector implementation in the Monte Carlo simulation. The systematic uncertainty of the tracking efficiency for the cuts used in this analysis was already studied in [75] using cut variations and was found to be 4%. In [76] the uncertainty of the momentum resolution was studied and estimated to be 20%. To estimate the influence of those uncertainties on the Monte Carlo correction factors a parametrised detector response is applied to PYTHIA generated events clustered with FastJet using the the anti-k_{T}-algorithm. This detector response is based on

a parametrisation of the tracking efficiency obtained from the full GEANT based detector simulation and a smearing of the transverse momenta of the particles. The p_{T}-dependent tracking efficiency is fitted in different subranges to obtain a section-wise defined parametrisation. In Fig. 4.2 the overall parametrisation of the tracking efficiency is shown for transverse momenta from 0 to 10 GeV/c (left panel) and 10 to 100 GeV/c (right panel).

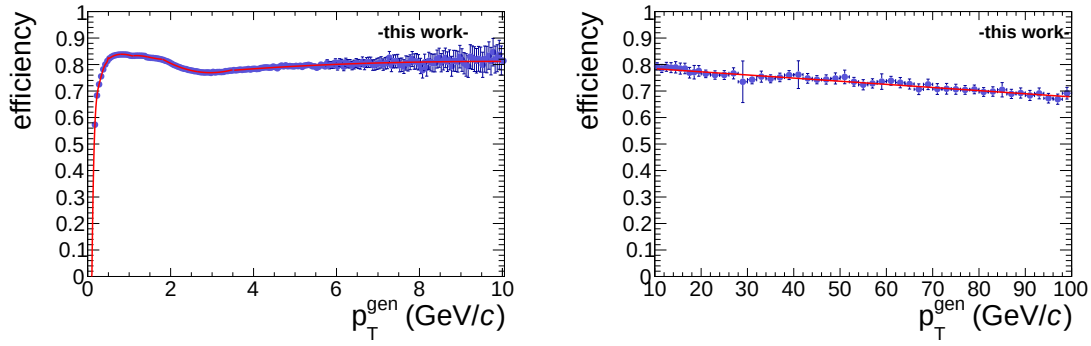

Figure 4.2: Parametrisation of the tracking efficiency (red curve) for particle momenta 0.15 to 10 GeV/c (left panel) and 10 to 100 GeV/c (right panel).

The transverse momentum smearing is based on a gaussian smearing of the inverse p_{T} with a width of $\sigma = 0.002$ (GeV/c)$^{-1}$. This width was determined in [77] using the Kalman Filter error estimate during the tracking procedure.

To estimate the systematic uncertainty we vary the parametrisation of the efficiency and the momentum resolution independently within the uncertainties mentioned in the beginning. We then finally derive the uncertainties from the difference of the bin-by-bin correction factors obtained from the varied parametrisation compared to those obtained from the reference parametrisation. This procedure is carried out for all used $p_{\mathrm{T,\,jet}}^{\mathrm{reco,\,ch}}$ bins to account for possible jet- and track-p_{T} dependencies. The systematic uncertainties are shown in Fig. 4.3.

The uncertainty of the efficiency is highest for low ξ values since the tracking efficiency at high track p_{T}induces jet p_{T}bin migration. At different ξ values the uncertainty is rather constant. We verified that sudden increases of this uncertainty for the highest ξ bin are due to the influence of statistical fluctuations in our fast simulation. The uncertainty of the momentum resolution is in general smaller than the uncertainty of the efficiency and contributes at all ξ values.

4.1.3 Total Systematic Uncertainty

To arrive at the total systematic uncertainty also other sources have to be taken into account. These uncertainties arise from the generator dependence of the bin-by-bin correction factors and uncertainties related to the description of secondary particle yields in the simulation.

The bin-by-bin correction relies on the correct description of the jet spectrum and fragmentation by the event generator. This uncertainty is not expected to be very large since in Sec. 4.2 we compare the simulation to our results and find that the data is reasonably well reproduced. However, this uncertainty has been studied in [73] using different MC generators and by artificially modifying the particle content of generated jets. The uncertainty was found to be largest ($\approx 5\%$) for small values of ξ and smallest ($\approx 1\%$) for high values of ξ, approximately independent of $p_{\mathrm{T,\,jet}}$.

In [73] the uncertainty related to the secondary correction has been studied using cut variations. It was found to be largest ($\approx 6\%$) for high values of ξ and smallest ($\approx 0.5\%$) for low values of ξ, also approximately independent of $p_{\mathrm{T,\,jet}}$.

To account for both uncertainties we add a conservative estimate of global 6 % to the obtained uncertainties.

A different systematic uncertainty arises from a possible residual trigger bias. At this point we do not assign an uncertainty for it. In Chapter 5 we discuss a possible method to quantify this bias.

All sources of systematic uncertainties are shown in Fig. 4.3 in a stacked representation. The uncertainty of a given source corresponds to the visible area in the plot. All those uncertainties are assumed to be uncorrelated and thus added in quadrature to arrive at the total systematic uncertainty.

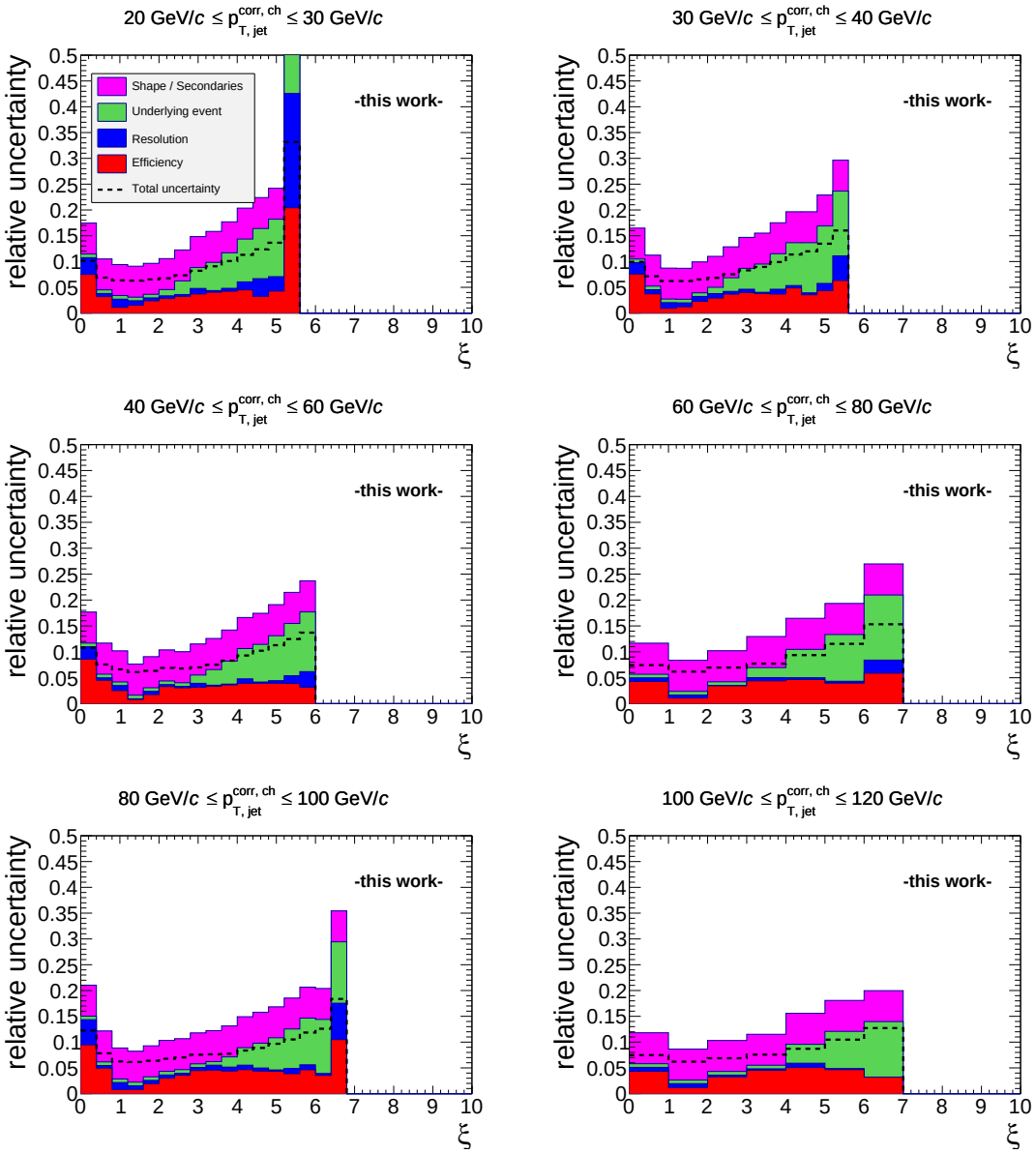

Figure 4.3: Relative systematic uncertainties for all $p_{\mathrm{T,\,jet}}^{\mathrm{reco,\,ch}}$ bins in stacked representation. Systematic uncertainty of given source corresponds to the visible area. The total uncertainty is calculated from the quadratic sum of the single uncertainties.

4.2 Final Results

In Fig. 4.4 we present the fully corrected fragmentation distributions for p-Pb collisions at 5.02 TeV in the momentum range 20 GeV/c to 80 GeV/c for minimum bias data and in the range 80 GeV/c to 120 GeV/c for TRD jet triggered data. We observe that for higher $p_{\mathrm{T,\,jet}}^{\mathrm{reco,\,ch}}$ the distributions extend to higher ξ values which is expected due to the smaller z values of given particles for higher $p_{\mathrm{T,\,jet}}^{\mathrm{reco,\,ch}}$. The slight increase in the area of the distribution indicates the increase in number of constituents for jets with higher transverse momenta. The particle yields are highest at intermediate ξ values and are suppressed at high ξ values. This leads to the so-called hump-backed plateau which is predicted by pQCD color coherence [78]. All observations are in qualitative agreement with prior findings for pp collisions at 7 TeV [73]. In Fig. 4.4 we also show a comparison to the particle level prediction of PYTHIA tune Perugia 2011 for pp collisions at 5.02 TeV and in Fig. 4.5 we show the ratio of those. We observe that the agreement to this PYTHIA reference is best for low to intermediate ξ values and gets worse towards the lowest and high ξ values. In these regions PYTHIA tune Perugia 2011 underestimates the particle content of the charged jets up to a factor of two for the highest ξ values. The same level of agreement to PYTHIA tune Perugia 2011 was found for pp collisions at 7 TeV for charged jets in the same transverse momentum regions between 20 GeV/c and 80 GeV/c [73].
We therefore conclude that charged jets in p-Pb collisions at 5.02 TeV show no significant modification in the longitudinal momentum distribution of particles compared to pp collisions. This observation is consistent with the absence of strong initial state or cold nuclear matter effects on the momentum distribution of particles in charged jets.
The ratio of the distributions from the TRD jet triggered data to the PYTHIA reference show the same shape as the minimum bias data, indicating the potential of these data. Due to the larger uncertainties they are found to agree with the reference. However, the charged jet fragmentation distributions for pp collisions have not been measured by the ALICE collaboration in this momentum region yet. Our 8 TeV pp detector level reference showed a good overall agreement with the p-Pb data in this transverse momentum region. In chapter 5 we will summarise this measurement and give an outlook to future measurements and studies.

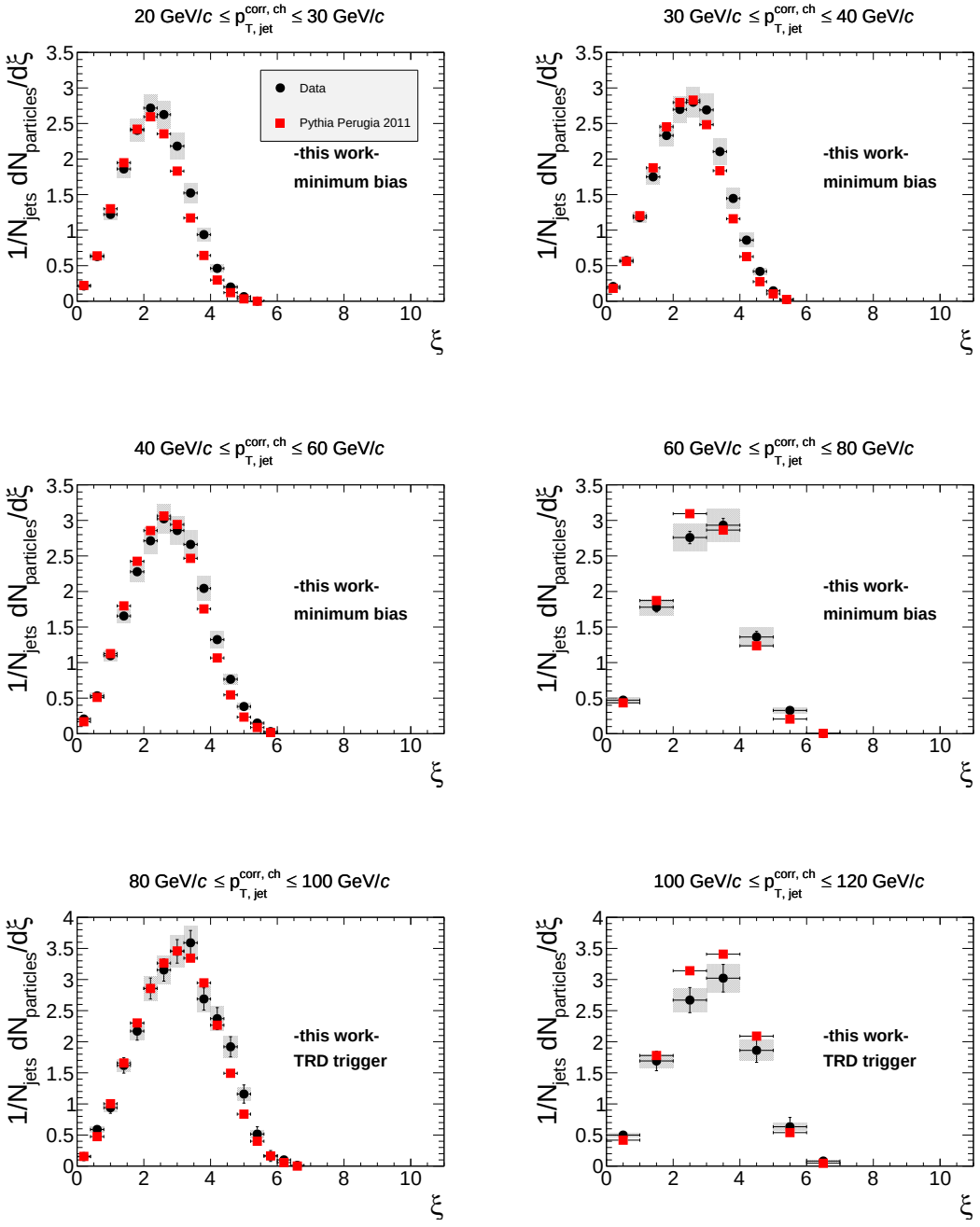

Figure 4.4: Fully corrected fragmentation distributions for p-Pb collisions at 5.02 TeV for minimum bias and TRD triggered data in the range 20 GeV/c to 120 GeV/c. Also a comparison to the PYTHIA tune Perugia 2011 pp prediction at 5.02 TeV is shown.

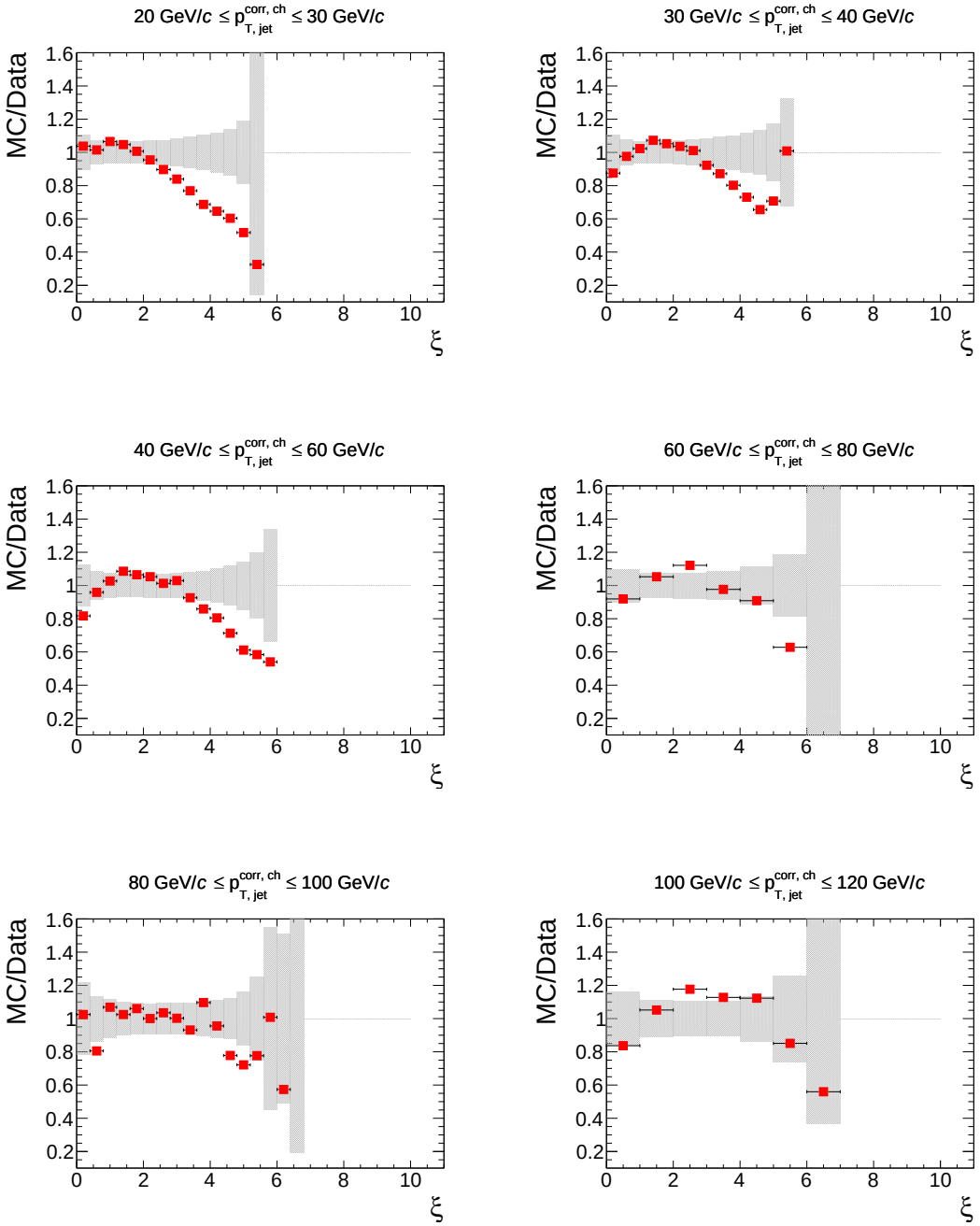

Figure 4.5: Ratio of PYTHIA Perugia 2011 pp predictions to measured distributions. The shaded area indicates the quadratic sum of the systematic and statistical uncertainty.

5 Summary and Outlook

In this work we presented the first measurement of jet fragmentation in p-Pb collisions with ALICE. The longitudinal momentum distribution of charged particles in charged jets was measured with minimum bias and TRD jet triggered data. The minimum bias data could be used to cover the lower charged jet transverse momenta up to 80 GeV/c. Using TRD jet triggered data the range of this measurement could be extended to $p_{\mathrm{T,\,jet}}^{\mathrm{reco,\,ch}} = 120$ GeV/c. The fragmentation distributions derived from TRD jet triggered data show a trigger bias at lower transverse momenta of the charged jets, due to the trigger condition of at least three tracks above a transverse momentum of 3 GeV/c in any TRD stack. Above 80 GeV/c no bias is visible in the fragmentation distributions which suggested to use them above this threshold for the measurement. Our finding is supported by a comparison of the fragmentation distributions derived from TRD triggered data and EMCal triggered data for pp collisions in [60] for the bin 80 to 100 GeV/c which shows a good overall agreement. To further investigate or quantify a possible residual bias a full TRD trigger simulation is needed. At the time the analysis was carried out such a simulation was not available, but could be requested in the future.
To correct the fragmentation distributions for the influence of the underlying event we introduced a subtraction method based on the evaluation of cones placed perpendicular in azimuth to the leading jet in a given event. From those cones the mean underlying event transverse momentum density was estimated event-by-event and subtracted jet-by-jet. The contribution of the underlying event to the measured fragmentation distributions was subtracted on the event ensemble level. The fragmentation distributions were corrected for the influence of tracking efficiency, momentum resolution and secondary particles using the bin-by-bin correction method. The correction factors were derived from a PYTHIA tune Perugia 2011 pp simulation propagated through the ALICE detector with GEANT. The influence of systematic uncertainties related to the underlying event subtraction and those related to tracking efficiency and momentum resolution were studied extensively.
The fully corrected fragmentation distributions for charged jets in p-Pb collisions were shown in the momentum range 20 GeV/c to 120 GeV/c together with the prediction from PYTHIA tune Perugia 2011 for 5.02 TeV pp collisions. The observed agreement between the data and the PYTHIA pp reference was found to be similar to the measurement for 7 TeV pp collisions in [73]. This led us to the conclusion that no modifications of the momentum distribution of particles in charged jets in p-Pb collisions due to initial state or cold-nuclear-matter effects are observed. This finding is consistent with previous measurements of charged jets in p-Pb collision by the ALICE collaboration [46], [47].

In [79] the CMS collaboration reports an enhancement in the charged particle R_{pPb} between 20 GeV/c and 100 GeV/c charged particle p_{T}, larger (reaching up to 1.3 - 1.4) than expected from Next-to-Leading Order pQCD calculations. They suspect that this effect could be due to a modified jet fragmentation in p-Pb caused by a larger fraction of quark jets. However, our work shows that the jet fragmentation is not modified in p-Pb, which could indicate a problem with their interpolated pp reference.
This shows how important reference measurements are to understand effects in different collision systems. With the measurement presented in this work we have established an important reference measurement for future PbPb collisions in LHC run II which will take place at almost the same center of mass energy of 5.1 TeV.

Appendix

A MC Correction Factors

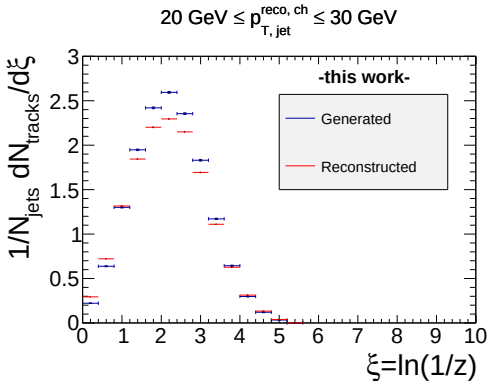

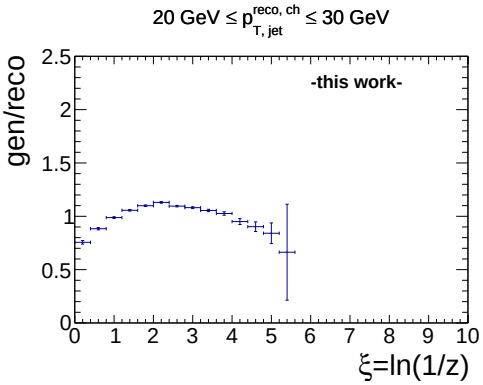

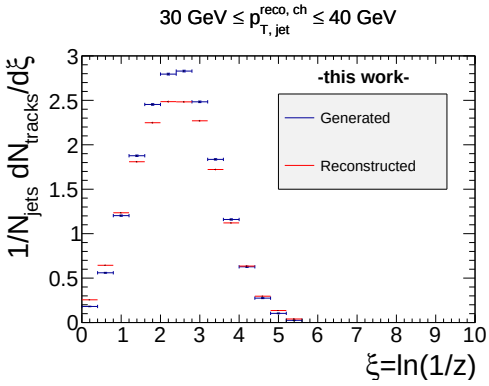

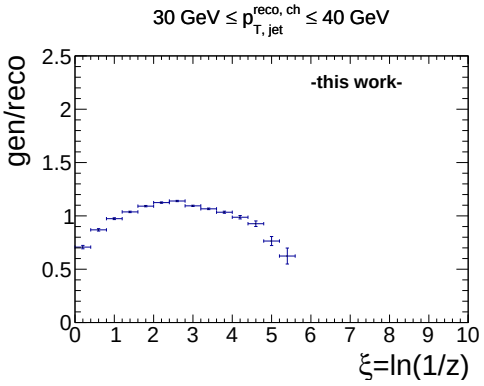

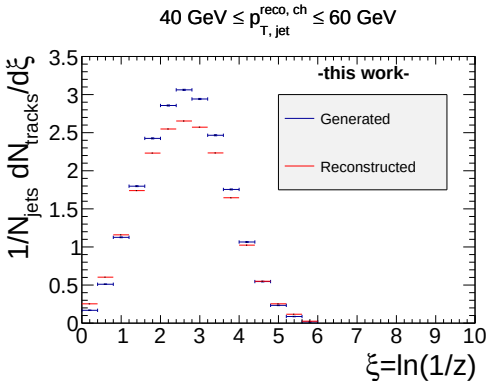

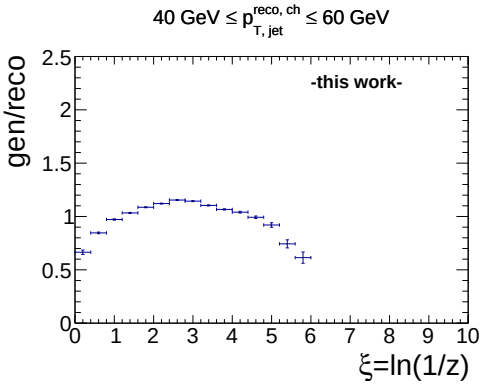

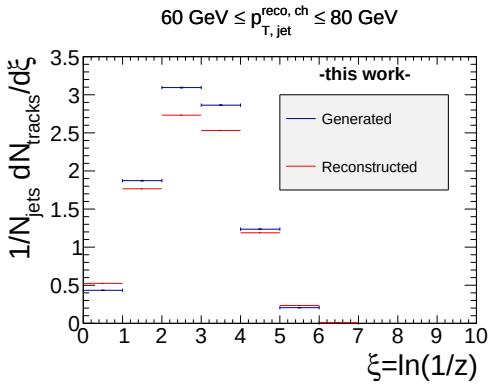
60 GeV ≤ p^reco, ch T, jet ≤ 80 GeV
-this work-
Generated
Reconstructed
1/N_jets dN_tracks/dξ
ξ=ln(1/z)

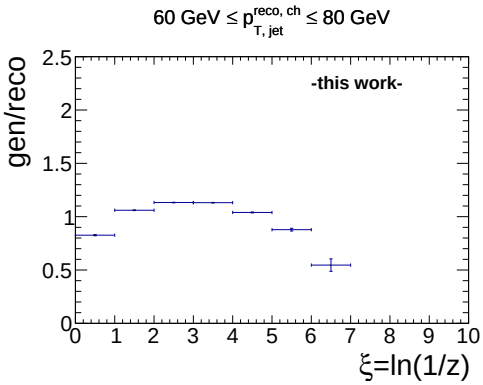
60 GeV ≤ p^reco, ch T, jet ≤ 80 GeV
-this work-
gen/reco
ξ=ln(1/z)

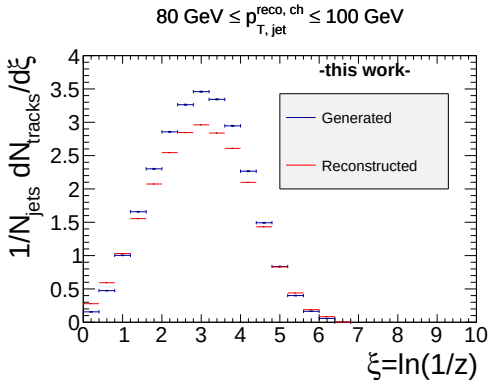
80 GeV ≤ p^reco, ch T, jet ≤ 100 GeV
-this work-
Generated
Reconstructed
1/N_jets dN_tracks/dξ
ξ=ln(1/z)

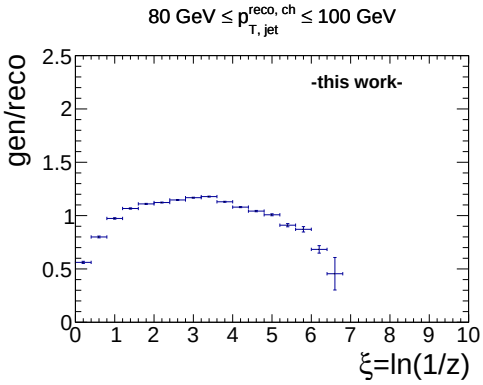
80 GeV ≤ p^reco, ch T, jet ≤ 100 GeV
-this work-
gen/reco
ξ=ln(1/z)

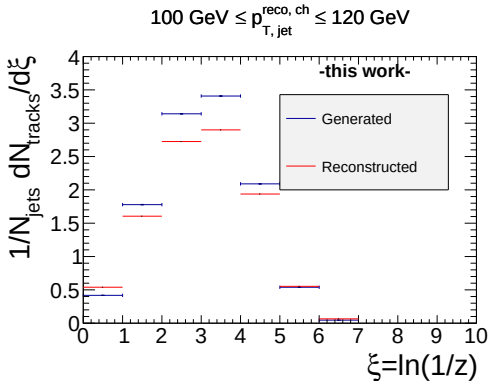
100 GeV ≤ p^reco, ch T, jet ≤ 120 GeV
-this work-
Generated
Reconstructed
1/N_jets dN_tracks/dξ
ξ=ln(1/z)

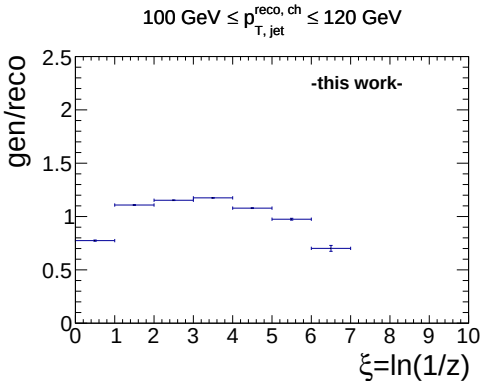
100 GeV ≤ p^reco, ch T, jet ≤ 120 GeV
-this work-
gen/reco
ξ=ln(1/z)

B List of Analysed Runs

B.1 pp

LHC12h pass 1
189122, 189146, 189228, 189229, 189231, 189306, 189310, 189315, 189316, 189350, 189351, 189352, 189353, 189397, 189400, 189402, 189406, 189407, 189409, 189410, 189411, 189603, 189605, 189610, 189611, 189612, 189616, 189621, 189623, 189647, 189648, 189650, 189654, 189656, 189658, 189696, 189697, 189698, 190209, 190210, 190212, 190214, 190215, 190216, 190240, 190303, 190337, 190338, 190340, 190341, 190342, 190386, 190388, 190389, 190390, 190392, 190393, 190416, 190417, 190418, 190419, 190421, 190422, 190424, 190425, 190895, 190898, 190903, 190904, 190968, 190970, 190974, 190979, 190981, 190983, 190984, 191129, 192004, 192072, 192073, 192075, 192095, 192128, 192136, 192140, 192172, 192174, 192194, 192200, 192201, 192202, 192205, 192246, 192344, 192347, 192348, 192349, 192415, 192417, 192453, 192461, 192468, 192471, 192492, 192499, 192505, 192510, 192729, 192731, 192732

B.2 p-Pb

LHC13b pass 3
195344, 195351, 195389, 195390, 195391, 195478, 195479, 195480, 195481, 195482, 195483

LHC13c pass 2
195529, 195531, 195566, 195567, 195568, 195592, 195593, 195596, 195633, 195635, 195644, 195673, 195675, 195677

LHC13e pass 2
196310, 196309, 196308, 196214, 196208, 196201, 196200, 196199, 196197, 196194, 196187, 196185, 196107, 196105, 196099, 196091, 196090, 196089, 196085, 195958, 195955, 195935

LHC13f pass 2
197388, 197387, 197386, 197351, 197348, 197342, 197341, 197302, 197300, 197299, 197298, 197297, 197296, 197260, 197258, 197255, 197254, 197247, 197189, 197184, 197150, 197142, 197139, 197138, 197092, 197091, 197015, 197012, 197011, 197003, 196974, 196973, 196972, 196967, 196965, 196722, 196721, 196706, 196702, 196701, 196648, 196608, 196535, 196477, 196475, 196474

C Lists

C.1 List of Figures

C.2 List of Tables

D Bibliography

[1] E. Rutherford. The scattering of α and β particles by matter and the structure of the atom. *Philosophical Magazine Series 6*, 21(125):669–688, 1911. URL: http://dx.doi.org/10.1080/14786440508637080.

[2] H. Yukawa. On the Interaction of Elementary Particles. *Proc. Phys.-Math. Soc. Japan*, 17, 1935. URL: http://web.ihep.su/dbserv/compas/src/yukawa35/eng.pdf.

[3] M. Gell-Mann. A schematic model of baryons and mesons. *Physics Letters*, 8(3):214 – 215, 1964. URL: http://www.sciencedirect.com/science/article/pii/S0031916364920013, doi:http://dx.doi.org/10.1016/S0031-9163(64)92001-3.

[4] J. E. Augustin et al. Discovery of a narrow resonance in e^+e^- annihilation. *Phys. Rev. Lett.*, 33:1406–1408, Dec 1974. URL: http://link.aps.org/doi/10.1103/PhysRevLett.33.1406, doi:10.1103/PhysRevLett.33.1406.

[5] J. J. Aubert et al. Experimental observation of a heavy particle j. *Phys. Rev. Lett.*, 33:1404–1406, Dec 1974. URL: http://link.aps.org/doi/10.1103/PhysRevLett.33.1404, doi:10.1103/PhysRevLett.33.1404.

[6] S. L. Glashow, J. Iliopoulos, and L. Maiani. Weak interactions with lepton-hadron symmetry. *Phys. Rev. D*, 2:1285–1292, Oct 1970. URL: http://link.aps.org/doi/10.1103/PhysRevD.2.1285, doi:10.1103/PhysRevD.2.1285.

[7] S. W. Herb, D. C. Hom, L. M. Lederman, J. C. Sens, H. D. Snyder, J. K. Yoh, J. A. Appel, B. C. Brown, C. N. Brown, W. R. Innes, K. Ueno, T. Yamanouchi, A. S. Ito, H. Jöstlein, D. M. Kaplan, and R. D. Kephart. Observation of a dimuon resonance at 9.5 gev in 400-gev proton-nucleus collisions. *Phys. Rev. Lett.*, 39:252–255, Aug 1977. URL: http://link.aps.org/doi/10.1103/PhysRevLett.39.252, doi:10.1103/PhysRevLett.39.252.

[8] F. Abe et al. Observation of top quark production in $\overline{p}p$ collisions with the collider detector at fermilab. *Phys. Rev. Lett.*, 74:2626–2631, Apr 1995. URL: http://link.aps.org/doi/10.1103/PhysRevLett.74.2626, doi:10.1103/PhysRevLett.74.2626.

[9] The ATLAS Collaboration. Observation of a new particle in the search for the Standard Model Higgs boson with the ATLAS detector at the LHC. *Phys.Lett.*, B716:1–29, 2012. arXiv:1207.7214, doi:10.1016/j.physletb.2012.08.020.

[10] The CMS Collaboration. Observation of a new boson at a mass of 125 GeV with the CMS experiment at the LHC. *Phys.Lett.*, B716:30–61, 2012. arXiv:1207.7235, doi:10.1016/j.physletb.2012.08.021.

[11] Wikipedia. Standard Model, February 2015. URL: http://en.wikipedia.org/wiki/Standard_Model.

[12] Sheldon L. Glashow. Partial-symmetries of weak interactions. *Nuclear Physics*, 22(4):579 – 588, 1961. URL: http://www.sciencedirect.com/science/article/pii/0029558261904692, doi:http://dx.doi.org/10.1016/0029-5582(61)90469-2.

[13] Steven Weinberg. A model of leptons. *Phys. Rev. Lett.*, 19:1264–1266, Nov 1967. URL: http://link.aps.org/doi/10.1103/PhysRevLett.19.1264, doi:10.1103/PhysRevLett.19.1264.

[14] Abdus Salam. Weak and Electromagnetic Interactions. *Conf.Proc.*, C680519:367–377, 1968.

[15] G. 't Hooft and M. Veltman. Regularization and renormalization of gauge fields. *Nuclear Physics B*, 44(1):189 – 213, 1972. URL: http://www.sciencedirect.com/science/article/pii/0550321372902799, doi:http://dx.doi.org/10.1016/0550-3213(72)90279-9.

[16] K.A. Olive and Particle Data Group. Review of particle physics. *Chinese Physics C*, 38(9):090001, 2014. URL: http://stacks.iop.org/1674-1137/38/i=9/a=090001.

[17] Yoshiaki Koma, Miho Koma, and Hartmut Wittig. Nonperturbative determination of the qcd potential at $o(1/m)$. *Phys. Rev. Lett.*, 97:122003, Sep 2006. URL: http://link.aps.org/doi/10.1103/PhysRevLett.97.122003, doi:10.1103/PhysRevLett.97.122003.

[18] R. Brandelik et al. Evidence for Planar Events in e+ e- Annihilation at High-Energies. *Phys.Lett.*, B86:243, 1979. doi:10.1016/0370-2693(79)90830-X.

[19] D.P. Barber, U. Becker, H. Benda, A. Boehm, J.G. Branson, et al. Discovery of Three Jet Events and a Test of Quantum Chromodynamics at PETRA Energies. *Phys.Rev.Lett.*, 43:830, 1979. doi:10.1103/PhysRevLett.43.830.

[20] Christoph Berger et al. Evidence for Gluon Bremsstrahlung in e+ e- Annihilations at High-Energies. *Phys.Lett.*, B86:418, 1979. doi:10.1016/0370-2693(79)90869-4.

[21] W. Bartel et al. Observation of Planar Three Jet Events in e+ e- Annihilation and Evidence for Gluon Bremsstrahlung. *Phys.Lett.*, B91:142, 1980. doi:10.1016/0370-2693(80)90680-2.

[22] Torbjorn Sjostrand, Stephen Mrenna, and Peter Z. Skands. PYTHIA 6.4 Physics and Manual. *JHEP*, 0605:026, 2006. arXiv:hep-ph/0603175, doi:10.1088/1126-6708/2006/05/026.

[23] Bo Andersson, G. Gustafson, G. Ingelman, and T. Sjostrand. Parton Fragmentation and String Dynamics. *Phys.Rept.*, 97:31–145, 1983. doi:10.1016/0370-1573(83)90080-7.

[24] Peter Z. Skands. QCD for Collider Physics. 2011. arXiv:1104.2863.

[25] John C. Collins, Davison E. Soper, and George F. Sterman. Factorization for Short Distance Hadron - Hadron Scattering. *Nucl.Phys.*, B261:104, 1985. doi:10.1016/0550-3213(85)90565-6.

[26] David d'Enterria. Jet quenching. *Landolt-Bornstein*, 23:471, 2010. arXiv:0902.2011, doi:10.1007/978-3-642-01539-7_16.

[27] David G. d'Enterria. Quark-Gluon Matter. *J.Phys.*, G34:S53–S82, 2007. arXiv:nucl-ex/0611012, doi:10.1088/0954-3899/34/7/S04.

[28] D.J. Schwarz. The first second of the universe. *Annalen der Physik*, 12(4):220–270, 2003. URL: http://dx.doi.org/10.1002/andp.200310010, doi:10.1002/andp.200310010.

[29] Wuppertal University. Das CBM Experiment an FAIR, February 2015. URL: http://astro.uni-wuppertal.de/html/Projekte/CBM.htm.

[30] Michael L. Miller, Klaus Reygers, Stephen J. Sanders, and Peter Steinberg. Glauber modeling in high energy nuclear collisions. *Ann.Rev.Nucl.Part.Sci.*, 57:205–243, 2007. arXiv:nucl-ex/0701025, doi:10.1146/annurev.nucl.57.090506.123020.

[31] Bengt Friman, Claudia Hohne, Jorn Knoll, Stefan Leupold, Jorgen Randrup, et al. The CBM physics book: Compressed baryonic matter in laboratory experiments. *Lect.Notes Phys.*, 814:1–980, 2011. doi:10.1007/978-3-642-13293-3.

[32] Sourav Sarkar et al. The Physics of the Quark-Gluon-Plasma. *Lect.Notes Phys.*, 785, 2010. doi:10.1007/978-3-642-02286-9.

[33] J.D. Bjorken. Energy Loss of Energetic Partons in Quark - Gluon Plasma: Possible Extinction of High p_T Jets in Hadron - Hadron Collisions. 1982. URL: http://lss.fnal.gov/archive/1982/pub/Pub-82-059-T.pdf.

[34] K. Adcox et al. Suppression of hadrons with large transverse momentum in central Au+Au collisions at $\sqrt{s_{NN}} = 130$-GeV. *Phys.Rev.Lett.*, 88:022301, 2002. arXiv:nucl-ex/0109003, doi:10.1103/PhysRevLett.88.022301.

[35] C. Adler et al. Centrality dependence of high-p_T hadron suppression in Au + Au collisions at $\sqrt{s_{NN}}$ = 130 GeV. *Phys. Rev. Lett.*, 89:202301, Oct 2002. URL: http://link.aps.org/doi/10.1103/PhysRevLett.89.202301, doi:10.1103/PhysRevLett.89.202301.

[36] Urs Achim Wiedemann. Jet Quenching in Heavy Ion Collisions. *Landolt-Bornstein*, 23:521–562, 2010. arXiv:0908.2306, doi:10.1007/978-3-642-01539-7_17.

[37] François Arleo. (medium-modified) fragmentation functions. *The European Physical Journal C*, 61(4):603–627, 2009. URL: http://dx.doi.org/10.1140/epjc/s10052-009-0871-z, doi:10.1140/epjc/s10052-009-0871-z.

[38] Nestor Armesto, Leticia Cunqueiro, Carlos A. Salgado, and Wen-Chang Xiang. Medium-evolved fragmentation functions. *JHEP*, 0802:048, 2008. arXiv:0710.3073, doi:10.1088/1126-6708/2008/02/048.

[39] Nicolas Borghini and Urs Achim Wiedemann. Distorting the hump-backed plateau of jets with dense QCD matter. 2005. arXiv:hep-ph/0506218.

[40] The CMS Collaboration. Measurement of jet fragmentation in PbPb and pp collisions at $\sqrt{s_{NN}}$ = 2.76 TeV. *Phys.Rev.*, C90(2):024908, 2014. arXiv:1406.0932, doi:10.1103/PhysRevC.90.024908.

[41] The ATLAS Collaboration. Measurement of inclusive jet charged-particle fragmentation functions in Pb+Pb collisions at $\sqrt{s_{NN}}$ = 2.76 TeV with the ATLAS detector. *Phys.Lett.*, B739:320–342, 2014. arXiv:1406.2979, doi:10.1016/j.physletb.2014.10.065.

[42] Larry D. McLerran. The Color glass condensate and small x physics: Four lectures. *Lect.Notes Phys.*, 583:291–334, 2002. arXiv:hep-ph/0104285, doi:10.1007/3-540-45792-5_8.

[43] C.A. Salgado, J. Alvarez-Muniz, F. Arleo, N. Armesto, M. Botje, et al. Proton-Nucleus Collisions at the LHC: Scientific Opportunities and Requirements. *J.Phys.*, G39:015010, 2012. arXiv:1105.3919, doi:10.1088/0954-3899/39/1/015010.

[44] A. Krzywicki, J. Engels, B. Petersson, and U. Sukhatme. Does a nucleus act like a gluon filter? *Physics Letters B*, 85(4):407 – 412, 1979. URL: http://www.sciencedirect.com/science/article/pii/037026937991284X, doi:http://dx.doi.org/10.1016/0370-2693(79)91284-X.

[45] Alberto Accardi. Final state interactions and hadron quenching in cold nuclear matter. *Phys.Rev.*, C76:034902, 2007. arXiv:0706.3227, doi:10.1103/PhysRevC.76.034902.

[46] The ALICE Collaboration. Measurement of charged jet production cross sections and nuclear modification in p-Pb collisions at $\sqrt{s_{\mathrm{NN}} = 5.02}$ TeV. 2015. arXiv:1503.00681.

[47] The ALICE Collaboration. Measurement of dijet $k_{\mathbf{T}}$ in p-Pb collisions at $\sqrt{s_{\mathbf{NN}}} = \mathbf{5.02}$ TeV. 2015. arXiv:1503.03050.

[48] Lyndon Evans and Philip Bryant. Lhc machine. *Journal of Instrumentation*, 3(08):S08001, 2008. URL: http://stacks.iop.org/1748-0221/3/i=08/a=S08001.

[49] ALICE. A Large Ion Collider Experiment, March 2015. URL: https://aliceinfo.cern.ch/.

[50] ALICE. Figure repository, March 2015. URL: https://aliceinfo.cern.ch/Figure/.

[51] The ALICE Collaboration. The alice experiment at the cern lhc. *Journal of Instrumentation*, 3(08):S08002, 2008. URL: http://stacks.iop.org/1748-0221/3/i=08/a=S08002.

[52] A Fantoni and the ALICE collaboration. The alice electromagnetic calorimeter: Emcal. *Journal of Physics: Conference Series*, 293(1):012043, 2011. URL: http://stacks.iop.org/1742-6596/293/i=1/a=012043.

[53] J Allen et al. ALICE DCal: An Addendum to the EMCal Technical Design Report Di-Jet and Hadron-Jet correlation measurements in ALICE. Technical Report CERN-LHCC-2010-011. ALICE-TDR-14-add-1, CERN, Geneva, Jun 2010. URL: https://cds.cern.ch/record/1272952.

[54] V I Man'ko, W Klempt, L Leistam, J De Groot, and Jürgen Schükraft. *ALICE Photon Spectrometer (PHOS): Technical Design Report*. Technical Design Report ALICE. CERN, Geneva, 1999. URL: http://cds.cern.ch/record/381432.

[55] Christian Wolfgang Fabjan, L Jirdén, V Lindestruth, Lodovico Riccati, D Rorich, Pierre Van de Vyvre, O Villalobos Baillie, and Hans de Groot. *ALICE trigger data-acquisition high-level trigger and control system: Technical Design Report*. Technical Design Report ALICE. CERN, Geneva, 2004. URL: http://cds.cern.ch/record/684651.

[56] The ALICE Collaboration. Performance of the ALICE Experiment at the CERN LHC. *Int.J.Mod.Phys.*, A29:1430044, 2014. arXiv:1402.4476, doi:10.1142/S0217751X14300440.

[57] Jochen Klein. Triggering with the ALICE TRD. *Nucl.Instrum.Meth.*, A706:23–28, 2013. arXiv:1112.5110, doi:10.1016/j.nima.2012.05.011.

[58] I. Antcheva et al. {ROOT} — a c++ framework for petabyte data storage, statistical analysis and visualization. *Computer Physics Communications*, 180(12):2499 – 2512, 2009. A celebratory issue focused on quality software for high performance, grid and novel computing architectures. URL: http://www.sciencedirect.com/science/article/pii/S0010465509002550, doi:http://dx.doi.org/10.1016/j.cpc.2009.08.005.

[59] ALICE. AliRoot, April 2015. URL: http://aliceinfo.cern.ch/Offline/.

[60] Jochen Klein. Jet Physics with A Large Ion Collider Experiment at the Large Hadron Collider. URL: http://inspirehep.net/record/1339771.

[61] R. Frühwirth. Application of kalman filtering to track and vertex fitting. *Nuclear Instruments and Methods in Physics Research Section A: Accelerators, Spectrometers, Detectors and Associated Equipment*, 262(2–3):444 – 450, 1987. URL: http://www.sciencedirect.com/science/article/pii/0168900287908874, doi:http://dx.doi.org/10.1016/0168-9002(87)90887-4.

[62] Matteo Cacciari, Gavin P. Salam, and Gregory Soyez. FastJet User Manual. *Eur.Phys.J.*, C72:1896, 2012. arXiv:1111.6097, doi:10.1140/epjc/s10052-012-1896-2.

[63] Matteo Cacciari, Gavin P. Salam, and Gregory Soyez. The Anti-k(t) jet clustering algorithm. *JHEP*, 0804:063, 2008. arXiv:0802.1189, doi:10.1088/1126-6708/2008/04/063.

[64] Stephen D. Ellis and Davison E. Soper. Successive combination jet algorithm for hadron collisions. *Phys.Rev.*, D48:3160–3166, 1993. arXiv:hep-ph/9305266, doi:10.1103/PhysRevD.48.3160.

[65] Matteo Cacciari, Gavin P. Salam, and Gregory Soyez. The catchment area of jets. *Journal of High Energy Physics*, 2008(04):005, 2008. URL: http://stacks.iop.org/1126-6708/2008/i=04/a=005.

[66] ALICE. Run condition table, May 2015. URL: https://alimonitor.cern.ch/configuration/.

[67] Jochen Klein. TRD trigger performance, May 2015. URL: https://twiki.cern.ch/twiki/pub/ALICE/TRDTriggers/an_trdtrg_v001.pdf.

[68] ALICE. Electronic Logbook, May 2015. URL: https://alice-logbook.cern.ch/logbook/.

[69] The ALICE Collaboration. Measurement of Event Background Fluctuations for Charged Particle Jet Reconstruction in Pb-Pb collisions at $\sqrt{s_{NN}} = 2.76$ TeV. *JHEP*, 1203:053, 2012. arXiv:1201.2423, doi:10.1007/JHEP03(2012)053.

[70] The ALICE Collaboration. Measurement of charged jet suppression in Pb-Pb collisions at $\sqrt{s_{NN}} = 2.76$ TeV. *JHEP*, 1403:013, 2014. arXiv:1311.0633, doi:10.1007/JHEP03(2014)013.

[71] Peter Zeiler Skands. Tuning Monte Carlo Generators: The Perugia Tunes. *Phys.Rev.*, D82:074018, 2010. arXiv:1005.3457, doi:10.1103/PhysRevD.82.074018.

[72] Rene Brun, Federico Carminati, and Simone Giani. GEANT Detector Description and Simulation Tool. 1994.

[73] The ALICE Collaboration. Charged jet cross sections and properties in proton-proton collisions at $\sqrt{s} = 7$ TeV. 2014. arXiv:1411.4969.

[74] The ALICE Collaboration. Centrality dependence of particle production in p-Pb collisions at $\sqrt{s_{\rm NN}}$= 5.02 TeV. 2014. arXiv:1412.6828.

[75] Ruediger Haake. Measurement of charged jet production in minimum bias p-Pb collisions at $\sqrt{s_{NN}} = 5.02$ TeV. *ALICE Internal Note*, 2015.

[76] The ALICE Collaboration. Centrality dependence of charged particle production at large transverse momentum in pb–pb collisions at. *Physics Letters B*, 720(1–3):52 – 62, 2013. URL: http://www.sciencedirect.com/science/article/pii/S0370269313000920, doi:http://dx.doi.org/10.1016/j.physletb.2013.01.051.

[77] Oliver Busch. Charged Particle Momentum Distribution in Jets. *ALICE Internal Note*, 2014.

[78] Yuri L. Dokshitzer, Valery A. Khoze, Alfred H. Mueller, and S.I. Troian. Basics of perturbative QCD. 1991.

[79] The CMS Collaboration. Nuclear effects on the transverse momentum spectra of charged particles in pPb collisions at $\sqrt{s_{\rm NN}} = 5.02$ TeV. 2015. arXiv:1502.05387.

Acknowledgements

Firstly, i would like to thank Johanna Stachel and Klaus Reygers for giving me the opportunity to join a highly active and interesting research field. I am grateful for all the comments on my work and for all the support that I experienced.
Also, I am deeply indebted to Oliver Busch and Jochen Klein for a lot of help and many fruitful discussions. Their passion for physics and their incredible teaching skills have inspired me since the first day.
I want to express my gratitude to Michael Winn for his constant interest in my work, many helpful discussions and for introducing me to the sport of canoeing. Many thanks go to Yvonne Pachmayr, Jeremy Wilkinson, Johannes Stiller and Alice Zimmermann for a lot of help in computing related issues.
I want to thank my office colleagues Martin Fleck and Ole Schmidt and also everybody else in the working group for the nice and pleasant atmosphere that i enjoyed over the last year.
For stable train operations and for solving train related issues i wish to thank Ana Marin, Silvia Masciocci, Filip Krizek, Joel Mazer and Marco van Leeuwen. Last but not least i want to thank Kai Schweda for ultrafast proofreading of my thesis and for providing a lot of motivation.

Deposition

Erklärung:

Ich versichere, dass ich diese Arbeit selbstständig verfasst habe und keine anderen als die angegebenen Quellen und Hilfsmittel benutzt habe.

Heidelberg, den 01.06.2015 .....